Geophysical Journal International

Geophys. J. Int. (2015) **200,** 863–879
GJI Gravity, geodesy and tides

doi: 10.1093/gji/ggu444

Integrated velocity field from ground and satellite geodetic techniques: application to Arenal volcano

Cyril Muller,[1,2] Rodrigo del Potro,[1,2] Juliet Biggs,[1] Joachim Gottsmann,[1] Susanna K. Ebmeier,[1] Sébastien Guillaume,[3] Paul-Henri Cattin[4] and Rodolfo Van der Laat[2]

[1] *School of Earth Sciences, University of Bristol, Wills Memorial Building, Queen's Road, Bristol BS*8 1*RJ, United Kingdom.*
E-mail: cyril.muller21@gmail.com
[2] *Observatorio Vulcanológico y Sismológico de Costa Rica, Universidad Nacional,* 2346-3000 *Heredia, Costa Rica*
[3] *Swiss Federal Institute of Technology Zurich, Geodesy and Geodynamics Lab, Robert-Gnehm-Weg* 15, *HPV G* 53, 8093 *Zürich, Switzerland*
[4] *University of Western Switzerland, Geomatic Faculty, Route de Cheseaux* 1, 1401 *Yverdon-les-Bains, Switzerland*

Accepted 2014 November 11. Received 2014 September 28; in original form 2014 May 5

SUMMARY

Measurements of ground deformation can be used to identify and interpret geophysical processes occurring at volcanoes. Most studies rely on a single geodetic technique, or fit a geophysical model to the results of multiple geodetic techniques. Here we present a methodology that combines GPS, Total Station measurements and InSAR into a single reference frame to produce an integrated 3-D geodetic velocity surface without any prior geophysical assumptions. The methodology consists of five steps: design of the network, acquisition and processing of the data, spatial integration of the measurements, time series computation and finally the integration of spatial and temporal measurements. The most significant improvements of this method are (1) the reduction of the required field time, (2) the unambiguous detection of outliers, (3) an increased measurement accuracy and (4) the construction of a 3-D geodetic velocity field. We apply this methodology to ongoing motion on Arenal's western flank. Integration of multiple measurement techniques at Arenal volcano revealed a deformation field that is more complex than that described by individual geodetic techniques, yet remains consistent with previous studies. This approach can be applied to volcano monitoring worldwide and has the potential to be extended to incorporate other geodetic techniques and to study transient deformation.

Key words: Time-series analysis; Spatial analysis; Satellite geodesy; Radar interferometry; Remote sensing of volcanoes; Volcano monitoring.

1 INTRODUCTION

Volcanoes deform due to a wide range of phenomena, which can be magmatic, hydrothermal, thermal or related to gravity loading, gravity instability or tectonic stresses (Dzurisin 2006). These phenomena can also occur simultaneously. Geodetic monitoring uses a variety of techniques, each of which has strengths and weaknesses, in terms of accuracy, spatial and temporal resolution, dimensionality, logistical costs and time span (Dvorak & Dzurisin 1997). These techniques measure ground deformation to identify volcanic and magmatic processes, with the goal of providing a better understanding of volcanoes and their associated hazards (Yang *et al.* 1992; Nunnari & Puglisi 1994; Pingue *et al.* 1998; Biggs *et al.* 2010b). Most studies tackle this by combining geodetic measurements within a source-specific geophysical model (e.g. Pritchard & Simons 2002; Battaglia *et al.* 2003; Biggs *et al.* 2010a; Manconi & Casu 2012), but this approach has several drawbacks when it comes to modelling multiple or complex sources. Furthermore, rheology must be assumed in advance and measurement noise is diluted by adjusting poorly constrained geophysical parameters such as Young's modulus. The goal of this paper is to combine and adjust the geodetic techniques within a rigorous reference system without a prior source model.

Previous studies such as Guglielmino *et al.* (2011), Samsonov & Tiampo (2006) and Wang & Wright (2012) have developed methodologies to combine InSAR and GPS into 3-D displacement or velocity surfaces. The novelty of this paper is to integrate a wider range of geodetic techniques commonly employed by volcano observatories such as EDM and spatial angles measured by a Total Station. This requires a more rigorously defined geodetic reference system, but also enables outliers to be identified and reduces the effects of correlated errors inherent to individual techniques. Moreover, we use the methodology to assess the geometry and accuracy of the geodetic network and provide recommendations for network design and optimisation, reducing logistical cost and increasing safety.

In the first section of this work, we review the main principles of the geodetic techniques commonly used by volcano observatories, and the mathematical basis by which measurements can be combined. The second section describes the new workflow and methodology. The third section describes the application to Arenal volcano where flank motion has been constant for the last few decades (Ebmeier *et al.* 2010; Avard *et al.* 2012; Feng *et al.* 2012; Mora *et al.* 2013) and geodetic techniques have been individually deployed. Finally, we discuss how the methodology can be extended to other measurement techniques and the mechanism that may be responsible for the deformation at Arenal volcano.

2 BACKGROUND

2.1 Geodetic techniques

Geodetic techniques used on volcanoes include Global Navigation Satellite System (GNSS), spatial distances, horizontal and vertical angles, levelling, photogrammetry, Light Detection And Ranging (LiDAR), tiltmeters, Interferometric Synthetic Aperture Radar (InSAR) and strainmeters. Table 1 lists the strengths and weaknesses of these geodetic techniques and describes their proprieties. We group these techniques into (1) spatial techniques, which capture the topography of the surface of the Earth and are spatially referenced and (2) temporal techniques, which require repeated acquisitions to provide a valuable result. Spatial techniques such as GNSS, Electronic Distance Measurement (EDM), can be linked into a single campaign of measurements (i.e. session), whereas tiltmeters, strainmeter and InSAR cannot. These two groups require two successive integrations in our methodology (i.e. spatial integration and spatio-temporal integration).

2.2 Reference system and reference frame

A unique reference system and a stable reference frame have to be defined in order to to combine different geodetic techniques. The reference system is a theoretical definition of a 3-D coordinate system which is designed to locate a point uniquely (e.g. International Terrestrial Reference System, ITRS). It is characterized by its origin, orientation and scale in a 3-D Euclidean space, it is sometimes associated with an ellipsoid and a projection. On the other hand, the reference frame is the practical application of the reference system and it is related to the field observations (e.g. very long baseline interferometry, GPS observations, satellite laser ranging) at a certain time (e.g. ITRF2008).

Different techniques used in volcano ground deformation monitoring may use different reference systems, which need to be transformed into a single reference system for the observation to be combined. For example, the results of GNSS post-processing are expressed in the ITRS which has its origin in the centre of mass for the Earth, its orientation parameters are given by the Bureau International de l'heure at 1984.0 and its scale is given by the SI unit of length: the metre. Whereas, horizontal and vertical angles are within a topocentric system where the origin is a point at the surface of the earth, the orientation is given by the direction of the gravity at this point and the geographic north and its scale is the metre. The topocentric system is more suitable for volcano monitoring because it maintains a similarity between field observations and the parameters of interest (e.g. displacement given in north, east and up are easily comprehensible; displacements in X, Y and Z geocentric are more confusing). The transformations of the observations between systems are rigorous and they do not affect accuracy.

In 3-D Euclidean space, reference frames are determined by 7 parameters (three translations, three rotations and one scaling factor). Individual geodetic measurements provide relative information between sites; together they form a geometry that has to be located in the reference system. Observations inherently fix some of the frame parameters, for example: 3-D distances fix the scale, GNSS baselines fix the orientation and the scale. The reference frame of the network needs to be estimated or fixed. It can be determined using the coordinates of the reference sites also called fiducial sites that are known in the reference system. For volcano monitoring applications, fiducial sites are typically located outside of the area

Table 1. Strengths and weaknesses of the main geodetic techniques used in volcano monitoring. Bold comments show the strengths while the italic indicates the weaknesses of each geodetic technique. Accuracy values are from equipment providers and the other values are from reasonable assumptions within the framework of volcano monitoring. Spatial distances, horizontal and vertical angles are called tacheometry because a modern Total Station comprises an EDM and a theodolite and they are recorded simultaneously.

Technique	Dimensionality	Accuracy	Coverage	Acquisition time consuming	Spatial resolution	Temporal resolution
GNSS campaign	**3-D**	2–5 mm + 0.3 ppm[a]	<50 km	8 hours/ site	*Single*	Campaigns
CGNSS	**3-D**	**2–8 mm**	**>1000 km**	**Installation and maintenance**	*Single*	**Daily/hourly**
Tacheometry	**3-D**	1 mm + 1 ppm[a]	<5 km	**Several sites per minute**	Several tens sites on the study area	Campaigns
Levelling	*1-D*	**0.5 mm km^{-1}**	**40–50 km**	*5–8* km d^{-1}	Few tens of sites	Campaigns
Tiltmeter	*2-D [μrad]*	**Several micro radian**	Few km	**Installation and maintenance**	*Single*	**Daily/hourly**
InSAR	*1-D (3D)*	1–2 cm	**1–50 km**	**No field work**	**>1000 points**	11–100 d
Strainmeter	*Strain 1-D/3-D*[b]	**0.005–1 μstrain**	**>50 km**	**Installation and maintenance**	*Single*	**Daily/hourly**
Photogram-metry/LiDAR	**3-D**	*10–20 cm*	**>100 km**	**Few minutes km^{-2}**	**10^9 points**	Campaigns

[a]ppm is part per million.
[b]1-D for volumetric strainmeter [e.g. Sacks-Evertson dilatational borehole strainmeter) or 3-D for multicomponent strainmeter (e.g. Sacks-Evertson tensor strainmeter; GTSM strainmeter)].

of interest and they define a local frame. Several different types of network adjustment can be used to include measurement within the reference frame:

(i) A 'free' network solution where the reference frame is strictly defined by the number of parameters that need to be estimated, for example a GNSS network by the nature of its observations fixes the scale and the orientation (three rotations). It therefore requires one fiducial site to determine the remaining three reference frame parameters (three translations). This type of solution relies on few fiducial sites and the network is not reliably fixed to the frame, therefore it is generally not suitable for a final result. However, it is useful to analyse the observations regardless of the heterogeneity of fiducial sites, so that measurement outliers (e.g. height of antenna wrongly reported, a badly aimed reflector, inadequate atmospheric model) can be identified, corrected or removed.

(ii) A 'loosely constrained' network solution determines the reference frame by using all the fiducial sites however the fiducial coordinates are introduced as observations in the adjustment. This solution assesses the inconsistency of the fiducial sites and detects relative motions between them. It may be used to define the reference frame when small inconsistencies between fiducial sites are detected.

(iii) A 'constrained' solution is when fiducial sites that are integrated in the adjustment, are larger than the strict minimum to define the reference frame, and measurements are constrained on the *a priori* coordinates or velocity of the fiducial sites. This step provides, in general, the final 3-D coordinates or velocities for all sites. Besides, it provides the final statistical estimators cited in Section 2.3.

Other adjustments using free network solutions with partial trace minimization, or loosely constrained solutions using the barycentre of the *a priori* and *a posteriori* coordinates of the fiducial sites exist (Dach *et al.* 2007; Guillaume *et al.* 2008) and determine the reference frame more or less consistently to assess observations, fiducial site discrepancies or to provide final solutions.

Unlike the transformation between reference systems, a change of frame is not always rigorous and may alter the accuracy of the observations. It is, therefore, crucial to define a reference frame that can be stable through time. Ideally, the geodetic datum is defined by several fiducial sites that are uniformly spread around the area of interest, observed for several years and that can be considered on a rigid tectonic block. The reference frame is thus defined by these fiducial sites.

Recent geodetic networks are usually made of GPS measurements however results from these measurements are provided in the International Terrestrial Reference Frame (ITRF) that account for plate motions and other mass movements. For volcanological applications, it is not convenient to assess displacement vectors contaminated by tectonic plate motions and in general, a local reference frame is defined. Two approaches are used to defined it: 'generalized constrain' approach when long time-series are available on the many fiducial sites and the 'finite constrained' approach when only short time-series on few fiducial sites are available (Lisowski *et al.* 2008; Palano 2010). In the first one, the secular velocities of the fiducial sites are computed within ITRF using a 'generalized constrain' solution (Dong *et al.* 1998) then the Euler pole parameters and eventually, a uniform strain rate are estimated and allow to reduce the site velocities from the tectonic block motion. Although, this solution is the most rigorous approach, a long time-series on uniformly spread fiducial sites cannot always be obtained. The second approach consists to constrain the measurements on the coordinates of fiducial sites that are determined in the first session of measurement, see Section 4.3.

2.3 Stochastical integration

Throughout the workflow of the methodology, the estimation of unknown parameters is completed with a generalized Gauss–Markov least square, also called a weighted least square (WLS), procedure (Menke 2012; Tarantola & Valette 1982; Welsch *et al.* 2000; Guillaume 2013). Based on the assumption that the observations are independent and Gaussian distributed, WLS provides the most likely solution (Caspary & Rüeger 1987; Welsch *et al.* 2000; Guillaume 2013). It estimates parameters, uncertainties for each site and the empirical accuracy for each measurement.

The observations are linked to the parameters within a mathematical model that is composed of both a functional and a stochastical model. The functional model is a set of equations describing the probabilistic behaviour of the observation, while the stochastical model is the set of equations that describes the statistical behaviour of the observations. Following linearization, the mathematical model is given by

$$\mathbf{l} + \mathbf{r} = \mathbf{A}\mathbf{x}, \tag{1}$$

where $\mathbf{l}$ is the vector of observations; $\mathbf{r}$ is the vector of residuals; $\mathbf{A}$ is the Jacobian matrix that links the observations to the parameters. $\mathbf{x}$ is the vector of the parameter, in this case, the point coordinates (east, north, altitude), GNSS translations/rotations, EDM scale, etc. The stochastic model is defined by the variance–covariance matrix:

$$\mathbf{C_{ll}} = \begin{pmatrix} \sigma_{l_1}^2 & \sigma_{l_1 l_2} & \cdots & \sigma_{l_1 l_n} \\ \sigma_{l_2 l_1} & \sigma_{l_2}^2 & \cdots & \sigma_{l_2 l_n} \\ \vdots & \vdots & \ddots & \vdots \\ \sigma_{l_n l_1} & \sigma_{l_n l_2} & \cdots & \sigma_{l_n}^2 \end{pmatrix}. \tag{2}$$

This allows us to compute the weighted matrix of observations:

$$\mathbf{W_{ll}} = \left(\frac{1}{\sigma_0^2} \mathbf{C_{ll}} \right)^{-1}, \tag{3}$$

where σ_0^2 is the variance of unit weight (i.e. $\sigma_0^2 = 1$). $\sigma_{l_i}^2$ and $\sigma_{l_i l_j}^2$ are the *a priori* variance and covariance values of the observations. If the observations l_i are assumed to be uncorrelated then the covariance is null and :

$$\mathbf{W_{ll}} = \begin{pmatrix} \frac{1}{\sigma_{l_1}^2} & 0 & \cdots & 0 \\ 0 & \frac{1}{\sigma_{l_2}^2} & \cdots & 0 \\ \vdots & \vdots & \ddots & \vdots \\ 0 & 0 & \cdots & \frac{1}{\sigma_{l_n}^2} \end{pmatrix}. \tag{4}$$

The most likely solution for $\mathbf{x}$ which minimizes $\mathbf{r^t W r}$ is given by:

$$\mathbf{X} = \mathbf{Q_{xx}} \mathbf{A^t W_{ll}} \mathbf{l}, \tag{5}$$

where

$$\mathbf{Q_{xx}} = (\mathbf{A^t W_{ll}} \mathbf{A})^{-1}. \tag{6}$$

An advantage of the WLS is that the $\mathbf{Q_{xx}}$ matrix (eq. 6) which contains the statistical value of each unknown, is created independently of the observations and only depends on *a priori* measurement uncertainties, $\mathbf{W_{ll}}$, and network geometry $\mathbf{A}$. Herein, it provides an

a priori estimation of the unknown accuracies that allows the optimization of the network configuration and the techniques to be used, before the network is surveyed, see Section 3.1.

Besides the estimation of the parameters, this procedure allows computation of useful estimators that enhance the detection of outliers and determine the quality of the output parameters (Welsch *et al.* 2000). The standardized residual error (WRMS residuals) is used to detect outliers according to the variance, the residual r_i is normalized within a centred Gaussian distribution $N(0, 1)$ as:

$$\mathbf{WRMS_{residual}} = \mathbf{r_i}/\sigma_0\sqrt{\mathbf{Q_{r_i r_i}}}, \tag{7}$$

where

$$\mathbf{Q_{rr}} = \mathbf{W^{-1}} - \mathbf{AQ_{xx}A^t}. \tag{8}$$

The threshold of rejection is commonly set at 3.5, which means that when the residual errors are under this value, they are contained within 99.9 per cent of the sample (Caspary & Rüeger 1987). The standardized residual errors allow a meticulous analysis of the adjustment and the detection of outliers. Moreover, this analysis is much more sensitive than the global chi-squared test, χ^2 (Menke 2012), because it allows each residual error value to be tested.

The overall empirical standard deviation of the whole data set allows the estimation of the accuracy of the adjustment, but the standard deviation of each parameter (for example, coordinates, velocities, rotations) can also be computed to provide more detailed information. These estimators are computed in two steps: first, the empirical standard deviation, s_0^2, is computed as:

$$s_0^2 = \frac{r^t \mathbf{W_{ll}} r}{(n-m)}, \tag{9}$$

where $n - m$ is the degree of freedom, number of observations minus number of parameters. Secondly, the accuracy of each parameter, $s_{x_i}^2$, can be estimated, using:

$$s_{x_i}^2 = s_0^2 \cdot Q_{x_i x_i}. \tag{10}$$

2.4 Arenal volcano

Arenal volcano is a 7 ka old, 1500 m high, basaltic-andesitic stratovolcano that has been persistently active through most of its history (Borgia *et al.* 1988; Soto & Alvarado 2006). It forms part of the recent Los Perdidos-Chato-Arenal complex located between the Tilaran Range to the south and the Guanacaste Range to the north (Borgia *et al.* 1988). After several hundred years of dormancy, Arenal erupted in 1968 July with a lateral blast on its western flank (Fudali & Melson 1971; Alvarado *et al.* 2006). This was the onset of a 42-yr-long eruptive period during which approximately 0.55 km^3 of lava dense rock equivalent (DRE) and pyroclasts erupted (Wadge *et al.* 2006).

Three new E–W aligned craters formed, named A, B and C, and the lava field was emplaced mainly on the western flank (see Fig. 1). Petrological studies suggest that this activity is fed by regular pulses of magma rising quickly from the mantle without evidence of shallow magma storage (Reagan *et al.* 1987; Streck *et al.* 2005). No effusive activity has been observed since the end of 2010.

Arenal has been showing continuous deformation for decades (Ebmeier *et al.* 2010; Avard *et al.* 2012; Feng *et al.* 2012; Mora *et al.* 2013). Ebmeier *et al.* (2010) analysed InSAR data between 2005 and 2009 and found a steady subsidence of the western flank of the edifice with a maximum rate of 70 mm yr^{-1} increasing from the foot of the edifice to about half way up the edifice, see Fig. 1. They tested the InSAR observations against a range of hypotheses, including a deflating magma source and the cooling and repacking of lava flows. They disregard most of these as primary mechanism and suggest that the mechanism causing the observed ground deformation is a gravity driven instability.

Mora *et al.* (2013) used a dry-tilt network around the volcano between 1986 and 2000 that showed a tilt toward the edifice, they reproduced the observed tilt data by loading the weight of the 1988–2000 emplaced lava field on an elastic basal layer. The addition of the deflation of a shallow-seated magma reservoir did not improve the quality of the fit to the observations.

Two other studies observed the deformation without suggesting geophysical mechanism. The volcano monitoring program run by the Observatorio Vulcanológico y Sismológico de Costa Rica (OVSICORI) used EDM to measure distance lines on the southern and western flank of the volcano for over two decades (1991–2012) and tiltmeters between 1976 and 2000 (GNV 1979–2000). The EDM times-series show a steady contraction with magnitudes between 1 and 7 cm yr^{-1} (Avard *et al.* 2012). Several μrad yr^{-1} of tilt towards the edifice were recorded at all sites. Feng *et al.* (2012) present GPS data from 1996 to 2010 for a network mainly designed to study the Nicoya Peninsula, that includes five sites around Arenal volcano (LOLA, AROL, PARK, WARN, GR38, see Fig. 1). The observed deformation pattern of the sites near Arenal shows a subsidence of a few millimetres per year with a horizontal velocity directed towards the volcano.

In summary, several geodetic techniques were deployed at Arenal volcano but the geophysical processes driving the deformation are still controversial, partly because of the different reference frame and spatial coverage of the different methods used. The long lasting and steady deformation makes Arenal volcano an ideal case to deploy, and improve the geodetic network using our proposed methodology.

3 METHOD

We propose combining geodetic observations from different techniques using a five-step workflow, illustrated in Fig. 2. As we explain in detail in the following sections, initially, we perform a simulation of the network using the prior uncertainties for each observation (see Section 2.3). After the acquisition and the post-processing, we adjust spatial measurements stochastically, session by session, into a single reference frame. Time-series are computed for each session as well as from InSAR measurements. Finally, results of both spatial and temporal time-series are integrated into a 3-D geodetic velocity field.

3.1 Network design and simulation

The literature on geodesy is broad and volcano monitoring is just one application, albeit with specific challenges. In particular, access for equipment installed is typically limited by volcanic hazard, terrain (water, vegetation and topography) or lack of infrastructure; monitoring areas are usually within complex tectonic settings that complicate the definition of a stable reference frame. Geodetic networks have to meet the requirements of monitoring and testing scientific hypotheses, but are also subject to logistical and safety constraints. The network design is the first and most important step in the methodology. In this step, the scientist chooses which techniques have to be used to reach the required accuracy, to cover the area of interest and to link the fiducial sites to the monitoring sites. This step is relevant to both new and pre-existing geodetic networks. In this section, we describe how to combine strengths of geodetic

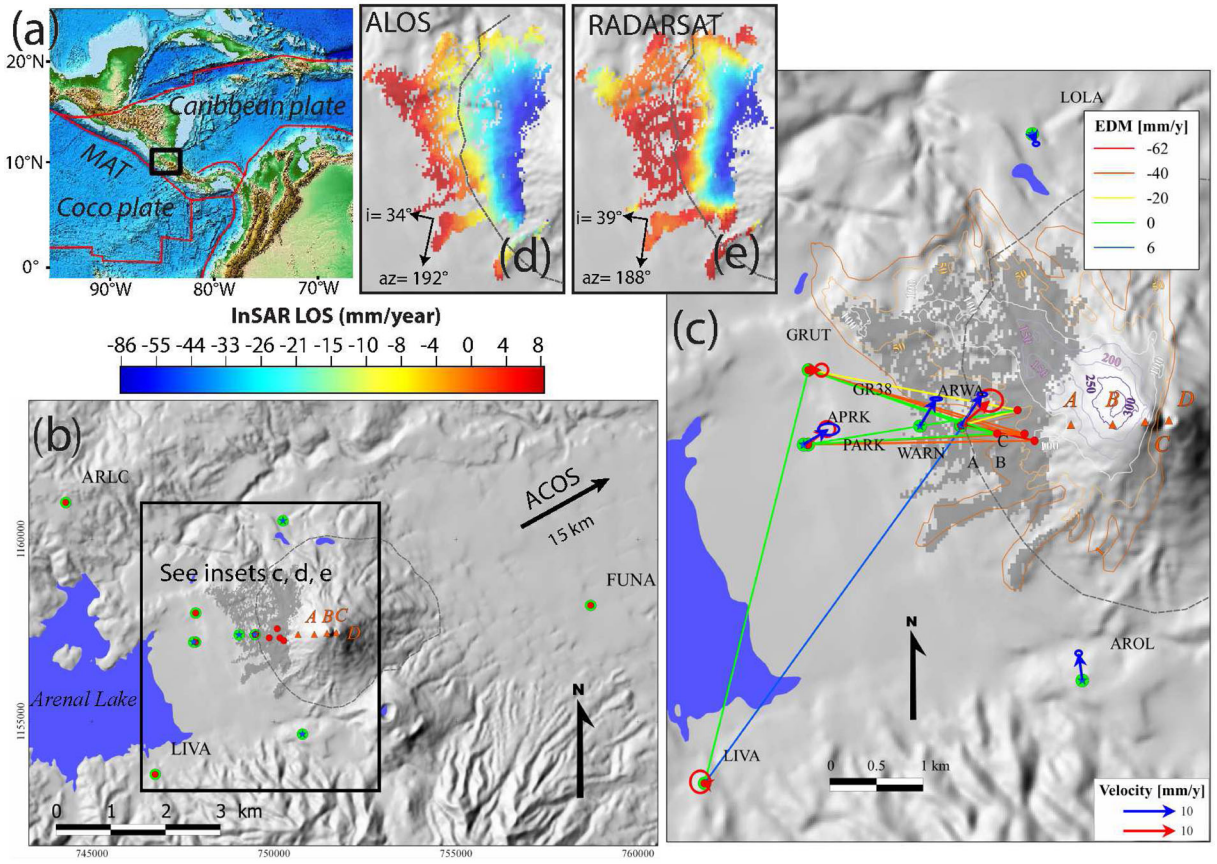

Figure 1. Arenal location, geodetic network and results of the times series of each individual geodetic technique: (a) regional tectonic settings: the Coco Plate subducts beneath the Caribbean Plate in the Middle American Trench (MAT). (b) Arenal volcano: the orange triangles are the 20th century craters of Arenal volcano. The red dots are the sites measured in this project, the reference frame of these velocities is defined by the ARLO and FUNA sites. The external green circles show the benchmarks measured with the GPS technique. The blue stars are the Feng *et al.* (2012) sites, the reference of these velocities is defined by the ACOS site (15 km NE of Arenal) located within the same tectonic unit. The dark grey area shows the extent of the area that is coherent in every RadarSat and ALOS interferogram from Ebmeier *et al.* (2010). The dashed grey line is the approximate foot of the volcano. (c) Zoom showing the sites on the western flank in more detail and the colour coded results of EDM times-series. Velocity vectors of each GPS data set with the associated velocities in red and their confidence ellipsoid at 95 per cent, to ensure the clarity of the map, we did not represent GPS vertical velocities. The contours show the lava thickness in meter from Wadge *et al.* (2006). (d) ALOS time-series from Ebmeier *et al.* (2010) with orbital parameter on left corner of the inset. (e) RADARSAT time-series from Ebmeier *et al.* (2010) with orbital parameter on left-hand corner of the inset.

techniques to improve the safety, cost effectiveness, coverage and overall accuracy.

A geodetic network that uses the strengths of each technique provides the most efficient volcano monitoring system. Remote techniques, like InSAR, photogrammetry and LiDAR or semi-remote ones such as tacheometry enable volcanologists to measure the edifice from a safe distance. More accurate techniques, such as CGNSS, tiltmeter, levelling, strainmeter and campaign, GNSS, are suitable in areas where the deformation signal and the volcanic threat are lower. Fiducial sites are used to separate volcano movements from non-volcanic deformation, such as local instabilities, regional faulting or tectonic displacements, which are common in volcanic areas (e.g. Jónsson *et al.* 1997; Diez *et al.* 2005; Gudmundsson *et al.* 2008; Takada & Fukushima 2013). These points must be located close enough to the volcano to avoid the corruption of the observations by unrelated movements, and yet out of the displacement field of the volcano. We use Arenal volcano as a case study, but our methodology could be applied to volcanoes worldwide.

The configuration of a geodetic network is often limited by accessibility, hazards and sometimes dense vegetation coverage. Here, we propose using clusters, which are small areas of interest spread around the volcano where topography and vegetation allow for a high density of sites (Fig. 3). The monitored clusters are linked to fiducial points with GNSS techniques, given to each cluster a position in the global reference frame. Each cluster needs at least a position and an orientation to be suitably georeferenced within the network and this is provided by two points measured with GNSS. LiDAR, photogrammetry, levelling, spatial distances, horizontal and vertical angles are used within each subarea to increase the density of measurements. The area over which InSAR measurement is possible is governed by satellite radar phase coherence, which is poor for areas with dense vegetation, areas of frequent rock-fall or steep slopes (Ebmeier *et al.* 2013). When possible, some 3-D sites should be set within the coherent area, which will give an absolute reference for InSAR displacements as well as improving the 3-D geodetic velocity field computation.

When the geodetic network is set up, an *a priori* simulation of one campaign can be carried out for the spatial techniques. Several commercial software packages carry out this type of adjustment, for example Panda, TRINET+, MOVE3, etc. Moreover, most equipment manufacturers such as Trimble Navigation Limited or Leica

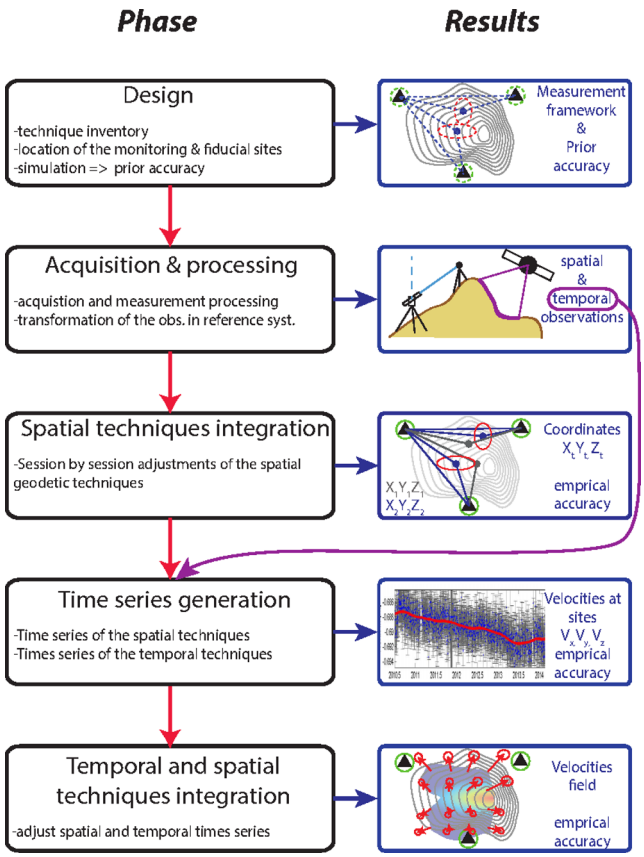

Figure 2. Workflow showing the combination of observations from different techniques in a five steps and the results of each step. We use the term spatial techniques for horizontal and vertical angles, spatial distances, levelling and GPS because they can be combined spatially in single session. We use the term temporal techniques for InSAR, tiltmeter and strainmeter because they can be combined in a spatio-temporal adjustment. The term tacheometry includes horizontal and vertical angles and spatial distances because they are acquired simultaneously with the same equipment.

geosystems AG also provide software that can adjust the geodetic network. These software packages provide an *a priori* accuracy of each parameter (e.g. coordinates, scale,. . .). Once *a priori* accuracies are obtained, velocity accuracies can be estimated for a number of sessions over the survey time. If a linear velocity is computed, the functional model linking coordinate observations to velocity is $y = vx + c$, where the unknowns are the velocity of each component (v) and the constant c. To solve for v and c we use eq. (5) in Section 2.3. For each site, the design matrix $\mathbf{A}$ is set with 6 columns representing 2 unknowns (v and c) for the 3 components (east, north, up). Each line of $\mathbf{A}$ matrix represents a campaign. The stochastic model represented by the diagonal matrix $\mathbf{W_{ll}}$, is filled with the coordinate accuracies that are provided by the commercial software. The simulation of the a priory velocities is computed with eq. (6). The simulated velocities are extracted from the Q_{xx} matrix with eq. (10) where $s_0^2 = 1$. The simulation based on geometry, accuracy, type and number of the observations provides *a priori* statistical estimators that assess whether the network is able, in terms of accuracy, to test the scientific hypothesis for the expected level of noise. Rigorous simulation is more useful for the combination of the techniques such as tacheometry and GNSS than for LiDAR, photogrammetry or InSAR because in the second group of techniques the internal accuracy (i.e. intrinsic measurement accuracy) is used.

3.2 Spatial integration and time-series

Following the acquisition and the transformation of the measurements within the reference system, the spatial geodetic techniques are combined through the three different types of adjustment described in Section 2.2. The validation of the three stages is done through the assessment of the WRMS residuals, described in the eq. (7). In the final adjustment, the global variance factor is assessed as well as the accuracies of each parameter, according to eqs (9) and (10). As for the *a priori* simulation, these adjustments are carried out using the same commercial software. The determination of a stable reference frame in the last step is crucial. When not many fiducial sites are available and time-series is short, a 'finite constrained' adjustment is chosen while in opposite situation a 'generalized constrained' and a dynamic reference frame are preferred, as explained in Section 2.2.

Once, both spatial techniques and temporal techniques results are obtained time-series are computed. Numerous methods exist for both 3-D point-based and temporal measurements, with the choice of method depending on the size of the data set and the complexity of the temporal deformation (e.g. Dong *et al.* 1998; Berrocoso *et al.* 2012; Fournier *et al.* 2009, or for InSAR Berardino *et al.* 2002; Hooper *et al.* 2004).

3.3 Spatial and temporal integration

Several approaches have been proposed for combining the high spatial resolution of InSAR with 3-D point-based GPS observations (Gudmundsson *et al.* 2002; Samsonov & Tiampo 2006; Guglielmino *et al.* 2011; Wang & Wright 2012). The methods of Gudmundsson *et al.* (2002) and Samsonov & Tiampo (2006) create an interpolated GPS field, and then integrate it with InSAR data by minimizing the Gibbs Energy function. The methods of Wang & Wright (2012) and Guglielmino *et al.* (2011) solve for both data sets simultaneously, avoiding the need for interpolation. The method of Wang & Wright (2012) is designed for continental-scale deformation accounting for orbital and topographically-correlated atmospheric delay and uses velocity field methods on a triangular mesh to produce a velocity field in the GPS reference frame with higher spatial resolution than is available from the sparse GPS data alone. The weighting of each observation type is contained within a Laplacian smoothing operator estimated using a scale-dependent umbrella operator. From this, the strain rates can be calculated directly. The method of Guglielmino *et al.* (2011) simultaneously inverts the InSAR and GPS data to calculate the strain tensor, the displacement field, and the rigid body rotation tensor for each point on a grid. Weighting of the observation types is determined by the measurement accuracy and the average distance between sites. Both methods provide a wider, more realistic deformation surface, but the Guglielmino *et al.* (2011) model uses weighting parameters with physical interpretations and is more suited to the volcanological context.

Here, we adapt the methodology of Guglielmino *et al.* (2011) to velocities instead of displacements following the method of Shen *et al.* (1996) and extend it from GPS velocities to all the 3-D point based velocities. Since no software is available to perform this integration, we describe the process in details.

Under the assumption of small, linear and homogeneous strain rate, the method computes the 3-D geodetic velocity of each pixel within a grid P, using all the N surrounding sites (EP) and the m InSAR line-of-sight (LOS) velocities for this pixel P, see Fig. 4. A least mean square adjustment is run independently for each pixel. The N surrounding EPs have the known coordinates

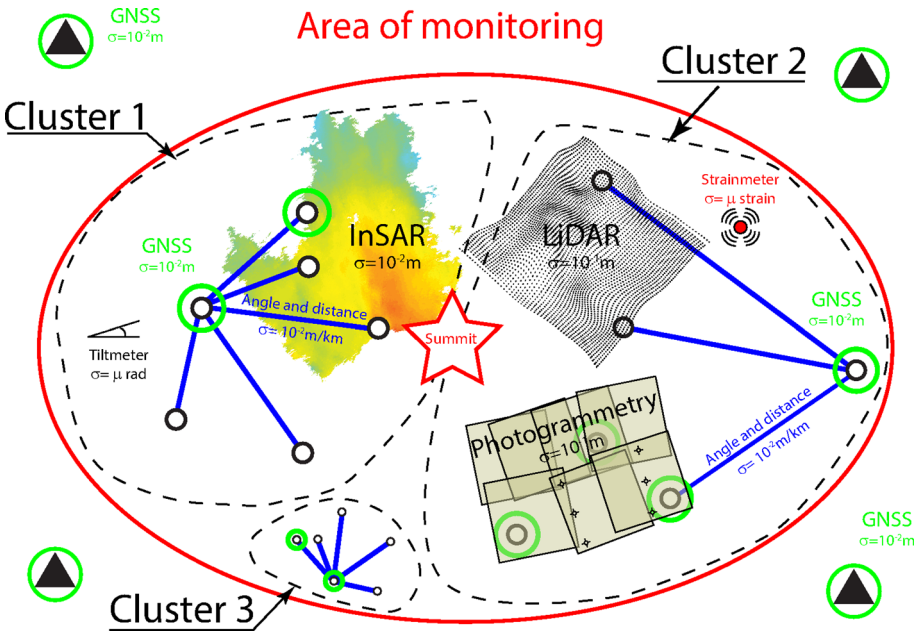

Figure 3. Example of a monitoring strategy using a multi-technique approach: the black triangles are the fiducial points, the black circles are the monitored sites, the green circles show the sites measured by GNSS and the blue lines show the relations between horizontal and vertical angles and spatial distances. The coloured area represents an InSAR image coverage. The dots show an area covered by LiDAR. The light green squares are the images taken by photogrammetry. The angle symbol is the tiltmeter and the red dot surrounded by several arcs is the strainmeter location. The dotted outlines indicate the several clusters that could be set considering factors such as the topography, access and risks.. Usually, a GNSS technique links the clusters and fiducial sites into the same reference frame.

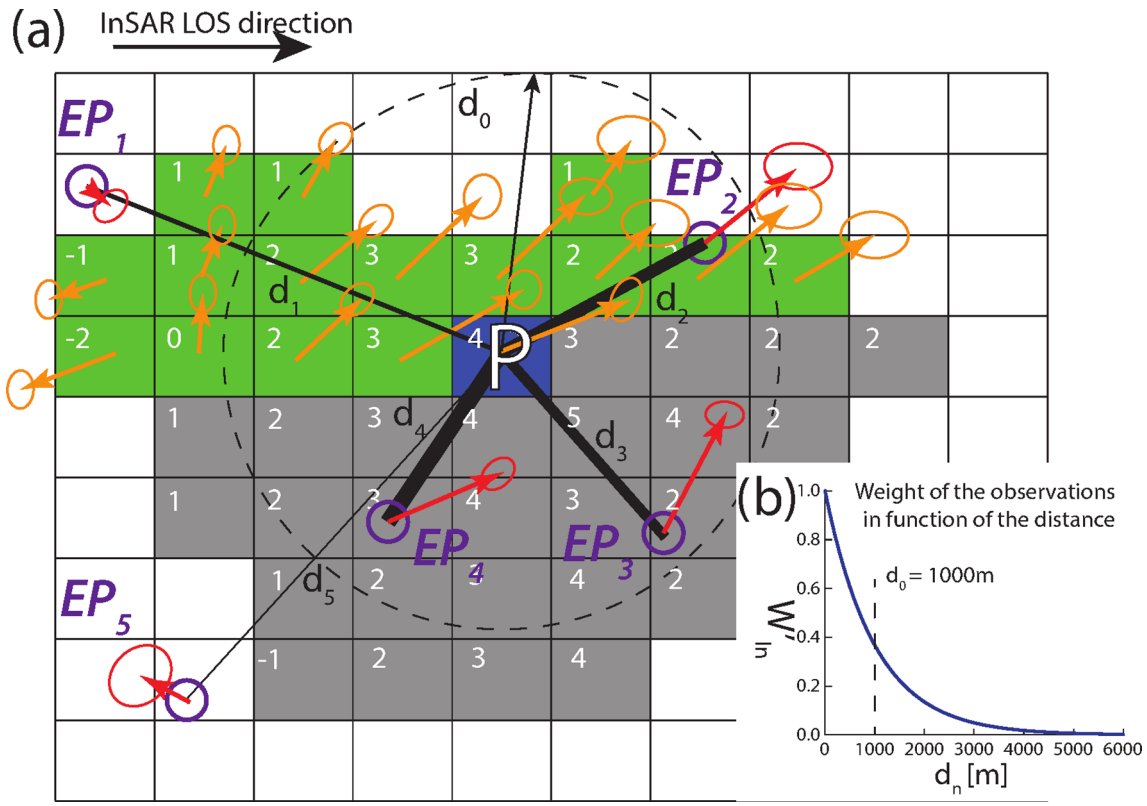

Figure 4. Spatial and temporal integration illustrating the calculation for given point, P. The filled pixels show the InSAR coverage with the value of the line-of-sight velocity. The pixels in green are already computed. The blue pixel, P, is the pixel currently being computed using the InSAR velocity, the velocities of the N EPs sites weighted with their distance to the pixel P. The grey pixels are the ones that need to be computed next. The red vectors are the discrete site velocities resulting from the time-series generation and the orange ones are the results of the spatial and temporal integration.

$\mathbf{x_{(n)}} = (x_n, y_n, z_n)$ and the known velocities $\mathbf{v_{(n)}} = (vx_n, vy_n, vz_n)$. The pixel P has the known coordinates $\mathbf{x_P} = (x_P, y_P, z_P)$ and the unknown velocity $\mathbf{V_P} = (Vx_P, Vy_P, Vz_P)$. The m InSAR measurements have the known velocities $\mathbf{v_m} = (vx_m s_{P,m}, vy_m s_{P,m}, vz_m s_{P,m})$ where $\mathbf{s_{P,m}}$ are the components of the unit vector pointing from P towards the satellite. Using these conditions, for each pixel, three equations are formed for each of the N surroundings *EP*s plus one equation for each of the m InSAR measurements. The functional model is written as:

$$\mathbf{v_{n,m}} + \mathbf{r} = \mathbf{H}\Delta\mathbf{x_n^P} + \mathbf{v_P}, \tag{11}$$

where the observations plus the residuals are equal to a linear function of the parameters, $\mathbf{H}$ and $\mathbf{v_P}$. $\Delta\mathbf{x_n^P} = \mathbf{x_n} - \mathbf{x_p}$ represents the spatial distance between the nth *EP* and the pixel P. $\mathbf{v_P}$ is the unknown velocity at the point P. $\mathbf{H}$ represents the gradient tensor which is the sum of the strain rate tensor matrix and the rigid body rotation rate tensor

$$\mathbf{H} = \begin{bmatrix} \dot{\epsilon}_{11} & \dot{\epsilon}_{12} & \dot{\epsilon}_{13} \\ \dot{\epsilon}_{12} & \dot{\epsilon}_{22} & \dot{\epsilon}_{23} \\ \dot{\epsilon}_{13} & \dot{\epsilon}_{23} & \dot{\epsilon}_{33} \end{bmatrix} + \begin{bmatrix} 0 & -\dot{\omega}_3 & \dot{\omega}_2 \\ \dot{\omega}_3 & 0 & -\dot{\omega}_1 \\ -\dot{\omega}_2 & \dot{\omega}_1 & 0 \end{bmatrix}. \tag{12}$$

Eq. (11) is linear and can be solved with a standard weighted least square adjustment. The functional model consists of an observed velocity vector:

$$\mathbf{v_{n,m}} = \begin{bmatrix} vx_{EP(1)} & vy_{EP(1)} & vz_{EP(1)} & \dots \\ vx_{EP(n)} & vy_{EP(n)} & vz_{EP(n)} & \dots \end{bmatrix}^t. \tag{13}$$

The design or coefficient matrix, $\mathbf{A}$, linking the parameters to the observations has a $3N + M$ lines with 12 columns corresponding to the 12 unknowns (Guglielmino *et al.* 2011). The $\mathbf{x}$ vector is the unknown vector of the point P parameters:

$$\mathbf{x_P} = [vx \quad vy \quad vz \quad \dot{\epsilon}_{11} \quad \dot{\epsilon}_{12} \quad \dot{\epsilon}_{13} \quad \dot{\epsilon}_{22} \quad \dot{\epsilon}_{23} \quad \dot{\epsilon}_{33} \quad \dot{\omega}_1 \quad \dot{\omega}_2 \quad \dot{\omega}_3]^t. \tag{14}$$

The second part of the mathematical model is the stochastic model, which is formed with the observation accuracy. The weight is computed in eq. (3), with the condition that *EP*s velocity observations are downweighted as a function of their distance to the pixel to be computed. These empirical expressions have been tested by Shen *et al.* (1996). The initial weight W_{l_n} is modified as:

$$\mathbf{W'_{l_n}} = \mathbf{W_{l_n}} e^{-d_{(n)}/d_0}, \tag{15}$$

where $d_{(n)}$ is the distance P to the nth *EP* and d_0 is a fraction of the average distance between *EP*s:

$$d_0 = \frac{1}{N * O} \sum_i^n d(ij), \tag{16}$$

where O is between four and six (Guglielmino *et al.* 2011). The weight of the EP velocity is $1/\sigma_{v_i}^2$ when distance $\Delta\mathbf{x_n^P}$ is null, see Fig. 4b); the weight is only a third of the initial one ($1/3\sigma_{v_i}^2$) when $\Delta\mathbf{x_n^P} = d_0$; at five times the d_0 the weight of the *EP* velocity is almost zero. It means that results are not influenced by *EP*s further than $5d_0$ from the pixel P.

To proceed with the computation, the area of interest is split into discrete pixels, and the parameters of each pixel are computed in an independent least mean square inversion. The $\mathbf{x}$ vector provides the 3-D velocities, strain rates and rotation rates for each pixel, which can be combined in a full 3-D geodetic velocity field.

4 APPLICATION

In this section, we apply the methodology previously described to the case study of Arenal volcano in Costa Rica where we assess the design of the geodetic network, the 3-D point-based stochastical adjustment and the integration results in a continuous deformation field for the period of 2008–2012.

4.1 Network design

From 2008 to 2012, we deployed a multitechnique geodetic network (GPS and tacheometry) on the western flank of Arenal volcano (see Table 2 and Fig. 1) to densify the existing network as well as to link the different geodetic techniques. Three fiducial sites were installed away from the volcanic system (FUNA, ARLO and LIVA) and nine sites were installed on the west flank of the volcano for monitoring (APRK, GRUT, ARWA, WARN, CASI, A, B, C and KOH). In our study, site WARN is located 30 m from benchmark ARWA, whereas Feng *et al.* (2012) employ a site named WARN which is referred in our study as ARWA. A, B, C, KOH, WARN

Table 2. Campaign summary with sites surveyed in each campaign and the techniques used (T, Tacheometry: horizontal and vertical angles, spatial distances and GPS) and the site type (MR is a mining reflector on >2 m^3 lava block or structure, SCS is a small buried concrete structure <2 m^3, BCS is on a big concrete structure such as a water tank or building.

Sites & their proprieties			Campaigns						
			03/2008	05/2008	06/2008	02/2009	03/2009	03/2012	05/2012
Cumulated time [year]			*0*	*0.2*	*0.3*	*0.9*	*1.0*	*4.0*	*4.2*
A	T+EDM	MR	x	x	x	x		x	x
APRK	GPS+T	SCS	x	x	x	x	x	x	x
ARLO	GPS	BCS	x	x	x	x	x	x	x
ARWA	GPS+T	SCS	x	x	x	x	x	x	x
B	T	MR	x	x	x	x		x	x
C	T	MR	x	x	x	x		x	
CASI	T	MR	x	x	x	x	———	destroyed	———
FUNA	GPS	BCS	x	x	x	x	x	x	x
GRUT	GPS+T	SCS	x	x	x		x	x	x
KOH	T+EDM	MR	[a]	x	x	x		x	x
LIVA	GPS+T	BCS	x	x	x	x		x	x
WARN	T	MR	x	x	x	x		x	x

[a]KOH observations of the first campaign were erroneous.

Table 3. Velocities of each benchmark after a time-series generation of the 3-D adjusted coordinates with their simulated and *a posteriori* accuracy. The velocity field residuals between the spatial technique integration and temporal and spatial technique integration agree with the final accuracy. The sites without residual are away from the velocity surface.

Benchmarks	Velocity			*A priori* accuracy			Empirical accuracy			3-D geod. vel. Field residual		
(mm)	East	North	Up	East	North	Up	East	North	Up	East	North	Up
Sites from this study												
A	–6	4	–20	3	4	6	3	5	7	–2	–1	–4
APRK	4	3	–5	3	3	5	1	1	4			
ARLO						——— Reference site———						
ARWA	6	5	–7	3	3	5	2	2	5			
B	–26	1	–64	3	6	8	3	6	7	2	0	9
C	–40	–5	–76	3	8	8	3	7	8	7	3	9
CASI	*17*	*11*	*–29*	*3*	*4*	*6*	*(22*	*34*	*58*	*–17*	*–6*	*15)*
FUNA						——— Reference site———						
GRUT	3	0	–8	3	3	6	1	1	3			
KOH[a]	*–13*	*7*	*–27*	*3*	*6*	*6*	*6*	*12*	*19*	*1*	*–4*	*–12*
LIVA	–1	0	–4	3	3	6	2	2	5			
WARN	6	5	–7	3	3	6	3	3	6	–3	0	1
Sites from Feng et al. (2012)												
ACOS						——— Reference site———						
AROL	–5	5	–5				1	2	3			
GR38	3	5	2				1	2	3	4	1	2
LOLA	5	–2	–5				1	2	3			
PARK	5	3	–1				2	4	8			
WARU	4	6	–4				1	2	6	1	–1	–1

Note: Problems appear along the acquisition of the sites in italic, therefore, simulated and posterior errors are not in agreement, see Table 2 for more details. Feng *et al.* (2012) sites do not have simulated accuracies because they were not integrated from the beginning in this study.
[a]KOH observations of the first campaign were erroneous.

and ARWA are located within the coherent area of Ebmeier *et al.*'s (2010) InSAR measurements and link the terrestrial techniques to the InSAR. We used GPS to link the reference points to three sites within the monitoring area (APRK, GRUT and ARWA), and then tacheometry to observe six remaining sites.

Using *a priori* observation uncertainties from equipment providers and TRINET+ software (Guillaume *et al.* 2008), we simulated the network configuration and assessed the point accuracy for a single session. *A priori* uncertainties are: for vertical and horizontal angles: 3″ arc second; for GPS east, north and up components: 4, 4 and 8 mm and for spatial distances: 1 mm + 1 part per million (e.g. at 5 km, accuracy is 1 + 5 = 6 mm). The sites that were positioned with both GPS and EDM had a prior standard deviation of ∼8 mm in both horizontal axes and ∼15 mm in vertical at 95 per cent confidence. The least accurate component of this network simulation was site C, which is high on the flank and thus only observed with the tacheometric method from ARWA, GRUT and APRK. It had an accuracy of 26 mm in the vertical component. The 95 per cent confidence ellipsoid error illustrates that for this point greater accuracy (8 mm) was obtained along the direction in which distances were observed, compared to both perpendicular directions (22 and 26 mm). The single session coordinate accuracies can be extended for velocity accuracy and we found that annual campaigns over the course of 4 yr provide a subcentimetric accuracy whenever velocities are steady (Table 3, see column *a priori* accuracy). The *a priori* accuracy for the area covered by InSAR is estimated from the variance of the detrended time-series, that is between 30 mm and 40 mm (Ebmeier *et al.* 2013).

In order to guarantee the reliability of our measurements, we applied the following scheme. Each point was observed for at least two days with GPS, or only one day with GPS and tacheometric measurements, or exclusively with tacheometry but from two different sites. The network can be occupied with five GPS receivers and one total station in 2 d. In comparison, the measurement of the same network using GPS exclusively would take 6–8 d (five receivers for 12 benchmarks for 2 d each and two common points between each session of 2 d) and would expose GPS equipments and scientist to areas of high volcanic threat. Moreover, this multitechnique network reduces the bias introduced by recurrent atmospheric effects present in GPS measurements (Dong *et al.* 2002; Chen *et al.* 2013; Grapenthin *et al.* 2013).

4.2 Acquisition and post-processing

4.2.1 Terrestrial observations from Arenal network

From 2008 February to 2012 June, we carried out seven campaigns. The first year, we executed three campaigns in 3 months to assess the repeatability of the network and its potential to detect small movements (expected displacement on site C is ∼2 cm). As results were encouraging, we continued measuring the network. In 2009, we carried out one complete campaign on all sites and one partial campaign which included five GPS sites but no tacheometry. The 2010 and 2011 annual campaigns were cancelled due to logistical issues. To overcome this problem and reach a subcentimetric accuracy for all points, we carried out two campaigns in 2012 (see accuracy Table 3).

The campaigns were carried out using five 1200 Leica geosystems double frequency receivers and one Total Station. In addition, a Leica DNA3 level was used to assess the local stability of the fiducial sites. Due to technical issues, we had to change the LEICA TC308 Total Station to a LEICA TM30 in 2012. In theory, the former allows for a much higher angle accuracy (±3″ arcdegrees) and distance meter accuracy (±1 mm+1 part per million) but we found the TC308 to be only slightly less accurate. We did not detect any scale or constant change between the two EDM instruments.

Angular and distance observations were recorded in series to partially eliminate axial instrumental error and hence improve the standard accuracy (Herubin 1978). Distances were corrected for temperature, pressure and humidity at the Total Station. GPS observations were processed with GAMIT software from the Massachusetts Institute of Technology (Herring *et al.* 2010). For each campaign, we used the coordinate from H-files generated by GAMIT, the loosely constrained daily solution (Cartesian coordinates in ITRF08) and considered them as measurements on TRINET+. This solution is not accurately referenced in ITRF2008 (the global reference frame) but the geometry formed by the network is strictly respected and it is not deformed by an eventual inhomogeneity between the ITRF2008 sites. This solution is ideal in our case because we are interested only in relative movements between fiducial sites and monitoring sites and not in integrating our measurements within a worldwide reference frame. The first loosely constrained estimation of 2008 March provides the coordinates of the fiducial sites (ARLO and FUNA).

We choose the topocentric reference system used in topography, photogrammetry and astronomy (Caspary & Rüeger 1987; Wendt & Dietrich 2003), which consists of a Cartesian reference system with its Z-axis following the direction of gravity at its origin. This reference system which is also called ENU, is chosen to minimize the complexity of the transformation applied to the observations and to provide easily understandable results. GPS and tacheometric measurements are transformed within this system before the adjustment (see the Appendix).

The Cartesian reference system's origin needed for the integration of observations was set on GRUT because this site is close to the barycentre of the network and thus keeps correction values on all sites small. We describe the transformation of the measurements to be in the topocentric reference system in the supplementary material, see Section A. Three corrections, N_i, V_O and V_i were needed on sites where vertical and horizontal angles were observed (i.e. GRUT, APRK, ARWA and LIVA). N_i is zero at the origin (GRUT) and $-142''$ (LIVA) arc degrees (this angle represents 70 cm at 1 km) in the northern component and $-37''$ (LIVA) and $+52''$ (ARWA) arc degrees in the east–west component. The low level of significance of the residuals on the vertical deflections (V_O and V_i) amongst the four sites justified the use of a unique value. The vertical deflection applied to each point was $16''$ arc degrees towards the north and null in the east–west component, with accuracy between respectively $2''$ and $5''$ arc degrees in the northern and the western component. This deviation represents the slope of the equipotential surfaces at the level of the network. In order to validate our vertical deflection values, we compared it with the CARIB97 geoid (Smith & Small 1999), which is the equipotential surface at sea level. Although both surfaces are not rigorously parallel, the comparison gave a maximum residual of a $4''$ arc degrees (0.001°). This first order comparison confirmed that our vertical deflection was correctly set.

4.2.2 *InSAR*

We use the InSAR results from Ebmeier *et al.* (2010), which used 28 interferograms from the RadarSat satellite ($\lambda = 5.6$ cm,) from 2005 December 29 to 2008 April 17 and six from ALOS satellite ($\lambda = 23$ cm track 466) from 2008 January 21 to 2009 April 25). InSAR measurements could only be made usefully from one viewing geometry (descending), because the western flank of Arenal is in part both obscured by its summit and foreshortened when viewed from ascending satellite geometry (Ebmeier *et al.* 2013). The extent of the InSAR data is limited by the poor coherence in the vegetated area surrounding the volcano and by steep, unstable slopes close to its summit, so that only parts of the post-1968 lavas of the volcano's western flank are coherent in all interferograms (data extent shown on Fig. 1). Interferograms were processed using the Repeat Orbit Processing software (ROIPAC) and topographic corrections made with Shuttle Radar Topography Mission (90 m resolution, Rosen *et al.* 2001).

4.2.3 *Nicoya GPS network*

Feng *et al.* (2012) provide velocities relative the Stable Caribbean Plate reference frame (DeMets *et al.* 2010). In order to compare them with the velocities of this study, we transform it in the same reference frame. For this purpose, we subtract the regional (i.e. Stable Caribbean Plate) from the local velocity (i.e. Arenal volcano surroundings). The site ACOS of Feng *et al.* (2012) is used as a reference site for the local velocity because it is out of the volcanic system and close to FUNA and AROL, our reference sites. Therefore, we compute the three translations to reduce the Stable Caribbean plate velocities to our local frame, in other words: the velocity of ACOS is subtracted at all the sites (Fig. 1). We validate the reference sites from both studies by comparing the velocities resulting from the times-series on two common sites and find that they can be considered mutually stable and part of the same tectonic unit.

4.3 Spatial integration

All spatial geodetic measurements acquired during our six campaigns over 4.5 yr were combined in a 3-D stochastic adjustment using TRINET+ (Schmidt 2006; Guillaume *et al.* 2008; Seube *et al.* 2012). We adjust the spatial measurement techniques following the standard procedure described in Section 3.2. An analysis of the residual of each campaign shows several measurements with high residuals. As the LOS passes close to the ground, the measurements between GRUT and KOH are noisy. During the two first campaigns, the residual values of the angles between GRUT and LIVA were recurrently higher than 3.5 (unitless). It appears that these high residuals result from the heating by the sun of a concrete structure close to GRUT generating vertical and lateral refraction. We measured these angles at night during the following campaigns.

The input of the coordinates of fiducial sites FUNA, ARLO and LIVA as measurements with a standard deviation of 5 mm in the 'loosely constrainted' adjustment does not reveal any significant relative movement (WRMS on the coordinates <3.5). However, LIVA shows a vertical residual just below the significance threshold, which was also detected by local relative levelling. We attribute this residual to a local instability. Although this residual is not significant yet, we do not want to deform the measurement network, therefore, we apply a finite constrained solution on FUNA and ARLO. These two points are the fiducial points for all displacements. LIVA is used as a check point to prevent drift or a rotation of the reference frame.

4.4 Time-series

Using multiple campaigns for each point, as well as the signal to noise ratio, allows us to compute a best-fitting linear velocity per site and per component for the observed period. Velocity accuracies are given by a linear regression and are similar to those given by the simulation, see Table 3. The results, shown in Fig. 5, show a significant downward movement of up to 70 mm yr^{-1} in site C,

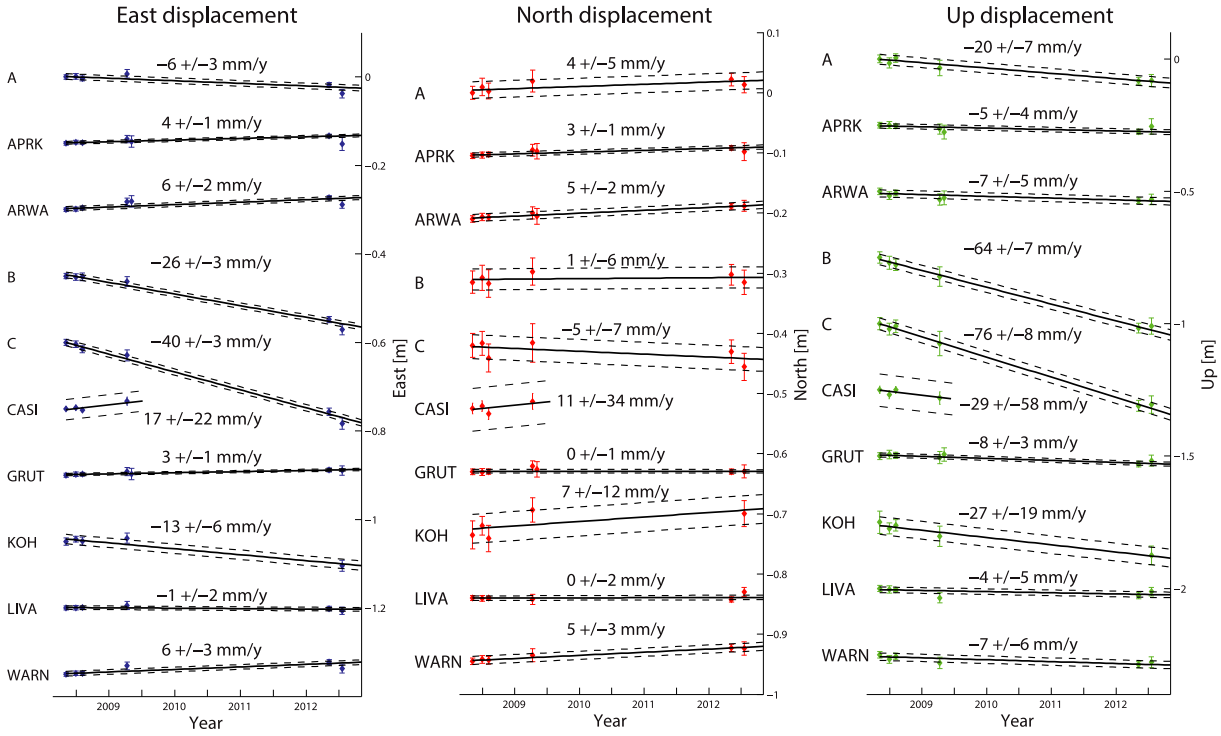

Figure 5. Time-series from the 2008 to 2012 campaigns in the east, north and up component. The values on top of each regression line are the velocities and their uncertainties. The error bars are the computed accuracies provided by the spatial integration in TRINET+. The dashed lines show the accuracy at 95 per cent for each regression. LIVA, the checkpoint, shows a relative stability during the period. ARLO and FUNA velocities are equal to zero as they are considered fixed through the observed period and are not displayed in this graph. Each position associated with uncertainties (1σ) of each session is computed within TRINET+ (spatial adjustment). The velocities are the results of a linear regression using the position (blue, red and green dots) and its accuracy. The accuracy display on the graph are the accuracies at 95 per cent ($\sim 2.5\sigma$ for each components) estimated in the linear regression. The values are computed as follow: $s^2_{\mathrm{vel}} = s^2_o \cdot Q_{x_i x_i}$, at 95 per cent $\Rightarrow 2.5 \cdot s_{\mathrm{vel}}$.

the highest benchmark on the flank. The subsidence decreases gradually down slope. At GRUT, APRK and ARWA, located where the gradient is nearly flat, we observe a subsidence of 5–8 mm yr^{-1}. The horizontal vectors show a maximum of 40 mm yr^{-1} westward at benchmark C and the movement progressively decreases down slope until it becomes null near CASI. A few hundred metres further west, which corresponds to the foot of the flank, the horizontal displacement changes direction from 6 mm yr^{-1} westward at ARWA and WARN to 3 and 4 mm yr^{-1} eastward at GRUT and APRK, respectively. The velocities at ARWA, WARN and APRK contain a north component between 5 and 3 mm yr^{-1}, decreasing towards the west direction. Although these north components are small, they are significant at 95 per cent confidence.

Time-series for both RadarSat and ALOS data were constructed using a least-squares inversion (e.g. Berardino *et al.* 2002; Lundgren *et al.* 2003), where velocities over the time intervals between SAR acquisitions were minimized (e.g. Berardino *et al.* 2002) and the deformation on the first acquisition date is assumed to be zero. Average deformation rates are then estimated from the total displacement of the resulting time-series. We treat uncertainties in these rates as the variance in time-series constructed from the average phase of an area east and upslope of WARN, relative to the westernmost edge of the coherent area: ± 36 mm yr^{-1} for the RadarSat data and ± 30 mm yr^{-1} for the ALOS data. Sources of uncertainty include phase contributions due to differences in satellite position and look angle, and most significantly, differences in atmospheric properties and composition on different acquisition days. Before the spatial and temporal integration, we assess the correlation between both InSAR time-series and the 3-D velocities (see Fig. 6). 3-D velocities are projected in the LOS of the two satellites using the satellites look vector parameters. Because InSAR is a relative measure only, offsets need to be computed for each InSAR data set. The LOS offsets are computed by minimizing residuals between the projected 3-D velocities at each site within the ground-based network and the InSAR observation (ALOS offset: –8 mm; RadarSat offset: –1 mm). The coefficient of correlations between 3-D velocities and both InSAR data sets is 0.99 and 0.96 for RadarSat and ALOS, respectively. The correlation is good and the data can then be integrated in a single velocity field.

Although velocities refer to the same fiducial sites, hence the same reference frame, the computed velocities from the different studies are not generated from the same reference system (i.e. UTM for GPS and InSAR and topocentric for spatial techniques). The difference in system is essential when coordinates or angles between sites are measured, but on centimetric velocity vectors the effect is negligible.

4.5 Spatial and temporal integration

Spatial velocities from this study and from Feng *et al.* (2012) are integrated with the InSAR velocities from both ALOS and RadarSat satellites. We exclude the site CASI that has been observed for less than a year as its velocity could not be considered reliable. We resample the InSAR data on a regular 20 m grid. The design matrix and measurement matrix are constructed as described in Section 3.3. The InSAR components of the weight matrix is built according to

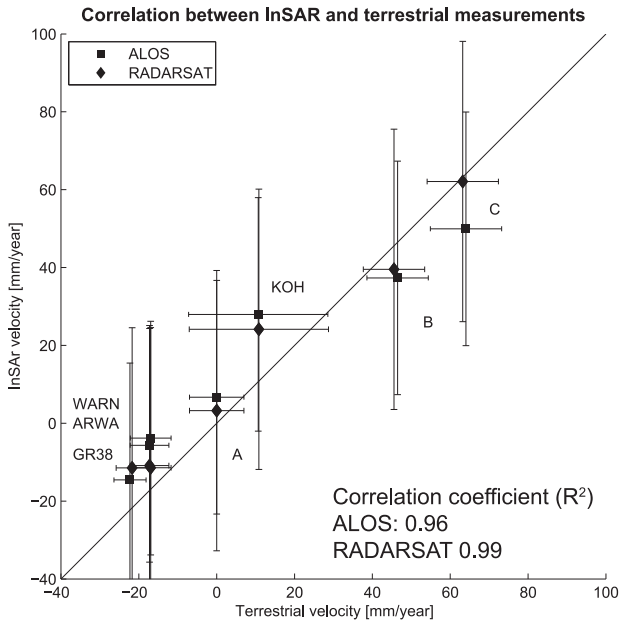

Figure 6. Graph showing the correlation between InSAR time-series velocities from ALOS and RadarSat and the 3-D benchmark velocity projected onto the line-of-sight (LOS) of each satellite. Squares represent ALOS and the diamonds represent RadarSat. ARWA, from this study, and WARN from Feng *et al.* (2012) are physically the same site. For clarity, only ARWA is shown in this graph. Note: the used sites are those within the InSAR coherence area.

InSAR velocity accuracy (σ_{InSAR}) taken from the time-series of Ebmeier *et al.* (2010), that is ±30 mm yr^{-1} for ALOS and ±36 mm yr^{-1} for RadarSat. Multitechnique velocity weights for the ground-based instruments are set from accuracy values (Table 3) and the equations of Shen *et al.* (1996). d_0 is ∼600 m but the value is reduced to 450 m to account for the strong velocity gradient between A and ARWA.

Fig. 7 shows the final 3-D geodetic velocity field. We limit the extent of the output velocity field using a threshold of the combined rms on the north, east and up components set at 1 $\sigma < 5$ cm, as well as the limit of the InSAR coverage. The deformation pattern at Arenal volcano presented here is much more complex than described by previous papers (Ebmeier *et al.* 2010; Avard *et al.* 2012; Feng *et al.* 2012; Mora *et al.* 2013), yet still in agreement with them. Fig. 8 shows that the overall accuracy is improved and the uncertainty does not exceed 25 mm yr^{-1} while InSAR alone has an accuracy ±36 and ±30 mm yr^{-1} for RadarSAT and ALOS, respectively. Two main areas of deformation are identified: the foot and the flank of the volcano. The foot has a statistically significant velocity up to 2 cm yr^{-1} pointing to the ENE with accuracy between few millimetre to 15 mm yr^{-1}. The vertical velocities show a significant subsidence of 1 cm yr^{-1} close to the slope. In the west part of the surface an uplift of 1 cm yr^{-1} slightly above of the significance threshold is detected. The second area has velocity magnitudes increasing from the bottom toward the summit of the volcano. The vertical subsidence is 2 ± 1 cm yr^{-1} at the bottom of the flank and reaches 10 ± 3 cm yr^{-1} at the eastern border of the deformation surface. Its horizontal velocities range from 1 ± 0.4 to 7 ± 3 cm yr^{-1} oriented westward.

Residual errors between point-based velocities and the velocity field are 1–12 mm yr^{-1} (see Table 3) while the residuals on InSAR velocities are between 25 and –57 mm yr^{-1} on ALOS observations and between 20 and –69 mm yr^{-1} for RadarSat data (see Fig. 9). The adjustment is considered good as none of the WRMS residuals are bigger than 3.5.

5 DISCUSSION

5.1 Improvements of the methodology

This paper describes an efficient workflow to combine geodetic observations in five steps: design and simulation of the geodetic survey, acquisition and processing, spatial integration, time-series generation and finally temporal and spatial integration. This methodology allows one to produce a unified 3-D geodetic velocity field from a combination of geodetic techniques commonly used on volcanoes. In the traditional procedure, geodetic observations are acquired independently and combined within a source specific geophysical model (e.g. Battaglia *et al.* 2003; Shirzaei & Walter 2010; Liu *et al.* 2011). Although, this strategy is simpler to set up and reduces the number of steps of the procedure, our methodology has numerous advantages.

First, the design of the network deployment allows the different geodetic techniques to be referenced in a unique reference frame. Moreover, it mitigates logistical cost by using the strengths of each technique. The simulation assesses whether the expected accuracy is optimal to detect the assumed geophysical process before any financial commitment needs to be made. At Arenal volcano, the design of a complementary network using GPS and tacheometry allows us to link the individual geodetic techniques previously deployed. It provides an absolute reference for the EDM observations of Avard *et al.* (2012) EDM and for the InSAR of Ebmeier *et al.* (2010). The effective combination of GPS and tacheometry on the complementary network reduces the logistic cost by 3 or even 4 compare to a single technique network. It also reduces the exposure of the scientists and expensive equipment to volcanic threats by using semi-remote technique (i.e. tacheometry) and remote techniques (i.e. InSAR) to observe the upper slopes. The presented geodetic network is the first step to improving the geodetic monitoring at Arenal volcano, and the current lack of coverage on the south, north and east flanks could be rectified by creating new clusters around the edifice that can be incorporated into the existing network.

Secondly, the simulated accuracy of GPS and tacheometric measurements is below ±1 cm yr^{-1}, this accuracy is attainable after 4 yr of steady deformation, considering one campaign per year. The accuracy of the *a posteriori* results agrees with the predicted velocity accuracy and hence highlights the usefulness of the method.

Thirdly, integration of the observation within stochastical least mean squares adjustment allows one to promptly identify outliers (e.g. atmospheric artefact, antenna or equipment offset) more reliably than the usual procedure because they cannot be absorbed by the uncertainty of geophysical parameters. As an example to illustrate this for the spatial integration of the Arenal network, the statistical estimators detect a persistent outlier in the tacheometric measurements between GRUTA and LIVA, this outlier was triggered by strong air refraction due to the heating of a concrete structure between the two sites. If geodetic techniques are deployed individually, such bias is difficult to identify. Moreover, the spatial integration allows a single campaign to be adjusted and tested; this has allowed us to take corrective action (i.e. night measurements) right after the second campaign without waiting for the geophysical modelling step.

Fourthly, the continuous 3-D deformation field provides an integrated deformation field, which improves interpretation and

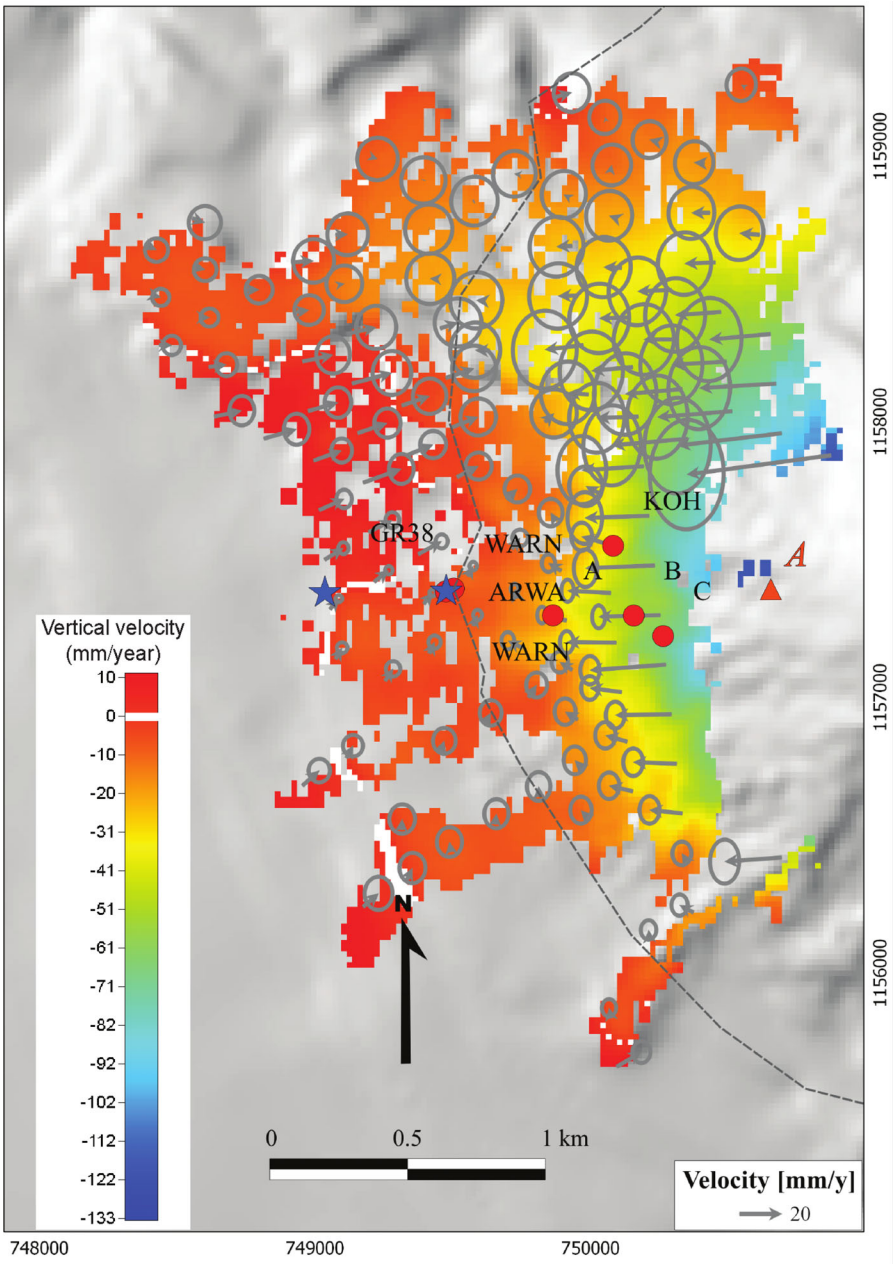

Figure 7. 3-D geodetic velocity field at Arenal volcano for the period 2008–2012. The grey arrows show the horizontal velocities (CGPS, GPS, horizontal and vertical angles, EDM, InSAR). The confidence ellipses are at 95 per cent. The coloured map shows the vertical velocity. The red dots are our geodetic sites and the blue stars are the geodetic sites from Feng *et al.* (2012). The orange triangle is one of the 20th century craters of Arenal volcano. The dashed grey line is the approximate foot of the volcano.

ultimately may allow more detailed geophysical modelling. At Arenal, the combination of all these data sets within a deterministic adjustment demonstrates the improvement. Using InSAR data as the sole monitoring component, the spatial extent of the data coverage is limited to the un-vegetated slopes of the volcano, moreover, although Ebmeier *et al.* (2010) combined measurements from both ascending and descending orbits, the north–south displacements are poorly resolved. The accuracy of the InSAR is estimated at ∼36 mm yr^{-1} while the integrated 3-D deformation surface results in an accuracy better than 25 mm yr^{-1}. When GPS and dry tilt (Feng *et al.* 2012; Mora *et al.* 2013) are used alone, it results in a low spatial coverage, because the volcanic activity prevents the installation of such equipment higher on the flanks. Both tacheometry (Avard *et al.* 2012) and InSAR suffer from the lack of an absolute reference and they cannot discriminate whether the flank, the foot of the volcano or both are moving. In terms of geophysical processes, Ebmeier *et al.* (2010) suggested a gravity instability as the primary mechanism and Mora *et al.* (2013) suggested loading. Our results shows that the mechanism may be invoke a more subtle mechanism, this is discussed in Section 5.3.

5.2 Method extension

In this section, we discuss possible extensions to the method to include tiltmeter and strainmeter observations as well as adaptations to non-linear velocities. In the case of Arenal volcano, the

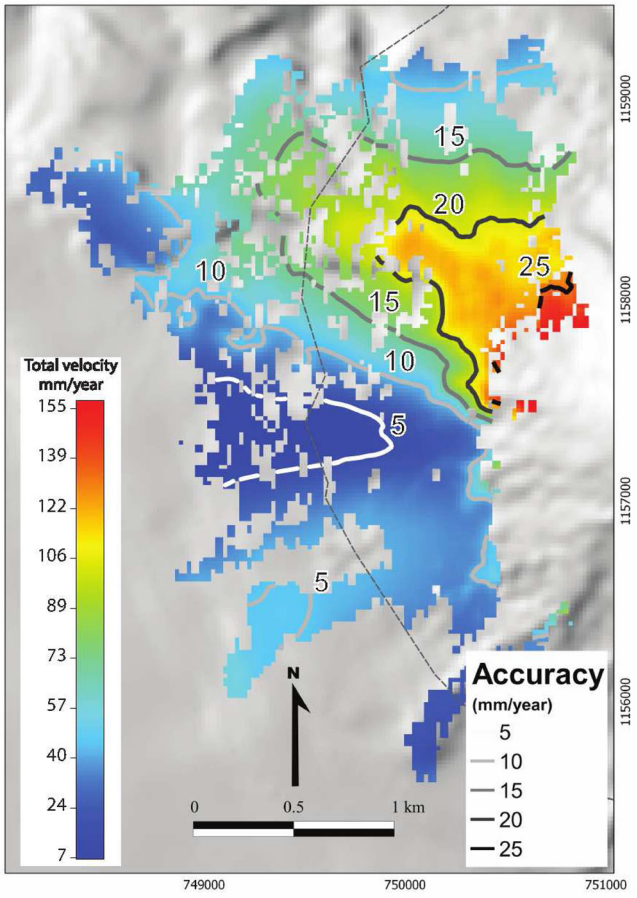

Figure 8. Norm of the velocity field with contours of accuracy at 95 per cent from 5 mm yr^{-1} (white) to 25 mm yr^{-1} (black). The dashed grey line is the approximate foot of the volcano.

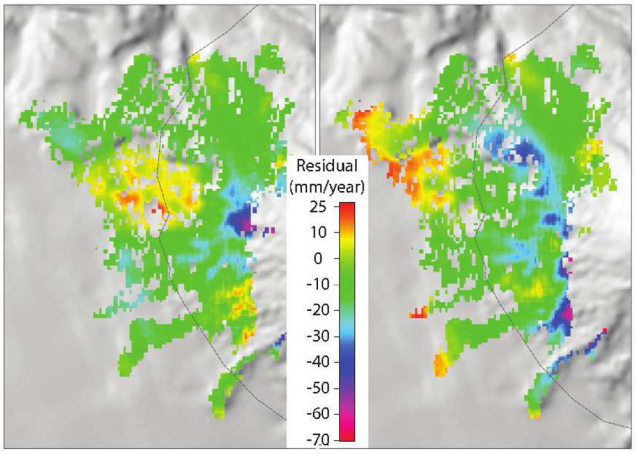

Figure 9. Residual between ALOS, descending InSAR on the left inset and RadarSat on the right inset, and the final results of the spatial and temporal technique integration. The dashed grey line is the approximate foot of the volcano.

deformation occurs at a constant rate, so it is appropriate to use a linear regression to compute the time-series. When velocities are not constant, the method could be extended using a Kalman filter (Dong *et al.* 1998; Fournier *et al.* 2009; Shirzaei & Walter 2010; Berrocoso *et al.* 2012).

Tiltmeters and strainmeters are similar to InSAR in the sense that they provide relative information between at least two sessions of measurement however, their results are not in units of length. Tiltmeters provide differential angles in two perpendicular directions (e.g. north and east) and strainmeters measure unitless changes in length or change in volume depending on the equipment used. The strain rate observations can be introduced directly as a measurement of the strain in eq. (11) of the 3-D geodetic velocity field computation. However, in the case of tiltmeters, observations are changes in the first derivative of the vertical displacement over time. One possibility is to transform angle rates into small elevation differences around the location of the tiltmeter. The equation producing the measurement at each point P of the grid is: $vz_n = (\alpha \delta x_n + \beta \delta y_n)$, where α and β are the tilt on the east and north axis. δx_n and δy_n are the components of the distance between the tiltmeter position and point P. In a case where the ground is uplifting without tilting, the tiltmeter would not be able to detect it. For this reason, the observation should be assigned an unknown vertical shift. This unknown shift can be determined better if, for example, the tiltmeter is set up with a CGPS station. In the same way that 3-D velocities at the EP benchmark are weighted, this measurement may be balanced depending on the distance. Further investigations to include a tiltmeter need to be carried out.

5.3 Geophysical interpretation of the deformation at Arenal

Previous studies have described: (i) a subsidence that is bigger on the flank than at the foot of the volcano (Ebmeier *et al.* 2010), (ii) a contraction of the distance between the foot and the flank (Avard *et al.* 2012) and (iii) a negative tilt toward the volcano (Mora *et al.* 2013). The processes invoked behind the observed deformation patterns are: (i) shallow gravity-driven instability and (ii) the elastic response of the loading of lava between 1988 and 2000. The deflation of a shallow magmatic source has been disregarded as primary mechanism by both Ebmeier *et al.* (2010) and Mora *et al.* (2013) and the existence of a shallow reservoir is contradictory to petrologic studies (Reagan *et al.* 1987; Streck *et al.* 2005).

The newly deployed geodetic network has been deployed on the western flank where previous geodetic data sets were available. In the terms of volcano geodetic monitoring, this network suffers from a lack of coverage on the eastern part of the volcano and may not capture the entire process however the deformation indicate that the deformation is mainly concentrate on the west part and reduce significantly on the south (AROL) and north (LOLA) of the edifice.

The combination of available geodetic measurements provides the following additional information: (i) the movement toward the volcano stops at the foot of volcano; (ii) the velocities on the west flank show a significant northern component and (iii) on the edifice, the deformation vectors are steeper (∼30°) than the slope of the volcano. This additional information provides evidence that none of the previously invoked processes can alone explain the observed deformation pattern. If flank instability occurs alone, the displacements on the base of the volcano should be zero and the velocities on the flank will tend to be parallel to the volcano slope (velocities: 65° to vertical; slope: 35° to vertical). Similarly, the simple loading of the post-1968 lava on a homogeneous elastic layer cannot explain the displacement of the flank of the volcano nor the long duration of the deformation.

Recent analytical models show that when material is loaded on top of two layers where the shallower is stronger than the underlying viscous layer, the stress on the edifice vicinity will tend to be

compressive and the displacement vectors will tend to be toward the edifice (Byrne *et al.* 2013). Moreover, the compression of the base of the edifice generates compression on the flank that triggers small and localized gravity instabilities. This scenario may correspond to the situation at Arenal where a weak, thick layer of Miocene sediments underlies a thin stronger layer of Plio-Pleistocene lavas (Pizarro 1993; Barboza *et al.* 1997; Alvarado *et al.* 2010). The loading of the post-1968 lava on a dual-layer basement, may be the primary deformation mechanism. Further investigation is required to test quantitatively this hypothesis.

6 CONCLUSION

An efficient combination of geodetic techniques in the same reference frame can improve volcano monitoring in terms of logistic costs, safety, accuracy and spatial and temporal coverage. The geodetic network at Arenal volcano shows that an *a priori* simulation is able to provide accuracy estimations before building the network, and the combination of GPS and tacheometry makes it possible to carry out safe and cost-effective campaigns. Finally, the adjustment of absolute point-based 3-D results with the high coverage of the LOS InSAR produces a more accurate, outlier-free 3-D deformation velocity surface without any source-specific assumptions. The methodology could be applied to many volcanoes worldwide where deformation monitoring exists or new geodetic networks need to be installed, to capture possible complex and subtle deformation patterns. The resulting enhanced ground deformation data may ultimately allow more detailed geophysical modelling of the processes driving the observed deformation. The Arenal example shows the improvement of the methodology over previously employed methodologies, and reveals a complex but constant ground deformation that might be caused by the loading of the post-1968 lava on a layered basement.

ACKNOWLEDGEMENTS

We thank Nicolas Fournier and Mimmo Palano for their constructive comments. We thank Francesco Guglielmino, as well as Sergey Samsonov for their advice and their explanations. This work received financial support from the Institute of Geomatics (heig-vd) through project 279 20172 Auscultation du Volcan Arenal, the University of Bristol, the Royal Society (UF090006), the NERC (NE/G01843X/1, NE/1015760/1), the EC FP7 under contract 282759 VUELCO, the European Commission under FP7 contract, the NERC/ESRC thematic programme STREVA and the NERC Centre for the Observation and Modelling of Earthquakes, Volcanoes and Tectonics (COMET).

REFERENCES

Alvarado, G.E., Carboni, S., Cordero, M., Avil, E. & Valverde, M., 2010. Stability of the cone and foundation of Arenal Volcano, Costa Rica, in *Volcanic Rock Mechanics: Rock Mechanics and Geo-Engineering in Volcanic Environments,* pp. 135–150, CRC Press, Taylor and Francis Group.

Alvarado, G.E., Soto, G.J., Schmincke, H.-U., Bolge, L.L. & Sumita, M., 2006. The 1968 andesitic lateral blast eruption at Arenal volcano, Costa Rica, *J. Volc. Geotherm. Res.,* **157**(1), 9–33.

Avard, G. *et al.*, 2012. *Volcanic activity in Costa Rica in 2012,* OVSICORI Official Annual Summary.

Barboza, G., Fernndez, J., Barrientos, J. & Bottazi, G., 1997. Costa rica: petroleum geology of the Caribbean margin, *SEG,* **30**(12), 1087–1090.

Battaglia, M., Segall, P., Murray, J., Cervelli, P. & Langbein, J., 2003. The mechanics of unrest at Long Valley caldera, California: 1. Modeling the geometry of the source using GPS, leveling and two-color EDM data, *J. Volc. Geotherm. Res.,* **127**(3), 195–217.

Berardino, P., Fornaro, G., Lanari, R. & Sansosti, E., 2002. A new algorithm for surface deformation monitoring based on small baseline differential SAR interferograms, *IEEE Trans. Geosci. Remote Sens.,* **40**(11), 2375–2383.

Berrocoso, M., Prates, G., Fernández-Ros, A. & García, A., 2012. Normal vector analysis from GNSSGPS data applied to deception volcano surface deformation, *Geophys. J. Int.,* **190**(3), 1562–1570.

Biggs, J., Lu, Z., Fournier, T. & Freymueller, J.T., 2010. Magma flux at Okmok volcano, Alaska, from a joint inversion of continuous GPS, campaign GPS, and interferometric synthetic aperture radar, *J. geophys. Res.: Solid Earth (1978–2012),* **115**(B12), doi:10.1029/2010JB007577.

Biggs, J., Mothes, P., Ruiz, M., Amelung, F., Dixon, T.H., Baker, S. & Hong, S.-H., 2010. Stratovolcano growth by co-eruptive intrusion: the 2008 eruption of Tungurahua Ecuador, *Geophys. Res. Lett.,* **37**(21), doi:10.1029/2010GL044942.

Borgia, A., Poore, C., Carr, M.J., Melson, W.G. & Alvarado, G.E., 1988. Structural, stratigraphic, and petrologic aspects of the Arenal-Chato volcanic system, Costa Rica: evolution of a young stratovolcanic complex, *Bull. Volcanol.,* **50**(2), 86–105.

Byrne, P.K., Holohan, E.P., Kervyn, M., van Wyk de Vries, B., Troll, V.R. & Murray, J.B., 2013. A sagging-spreading continuum of large volcano structure, *Geology,* **41**(3), 339–342.

Caspary, W.F. & Rüeger, J.M., 1987. *Concepts of Network and Deformation Analysis,* Vol. 11, University of New South Wales.

Chen, Q., van Dam, T., Sneeuw, N., Collilieux, X., Weigelt, M. & Rebischung, P., 2013. Singular spectrum analysis for modeling seasonal signals from GPS time series, *J. Geodyn.,* **72,** 25–35.

Dach, R., Hugentobler, U., Fridez, P. & Meindl, M., 2007. *Bernese GPS software version 5.0,* Astronomical Institute, University of Bern.

DeMets, C., Gordon, R.G. & Argus, D.F., 2010. Geologically current plate motions, *Geophys. J. Int.,* **181**(1), 1–80.

Diez, M., La Femina, P.C., Connor, Charles B., Strauch, W. & Tenorio, V., 2005. Evidence for static stress changes triggering the 1999 eruption of Cerro Negro volcano, Nicaragua and regional aftershock sequences, *Geophys. Res. Lett.,* **32**(4), doi:10.1029/2004GL021788.

Dong, Danan, Herring, TA. & King, R.W., 1998. Estimating regional deformation from a combination of space and terrestrial geodetic data, *J. Geod.,* **72**(4), 200–214.

Dong, D., Fang, P., Bock, Y., Cheng, M.K. & Miyazaki, S., 2002. Anatomy of apparent seasonal variations from GPS-derived site position time series, *J. geophys. Res.: Solid Earth (1978–2012),* **107**(B4), doi:10.1029/2001jb000573.

Dvorak, J.J. & Dzurisin, D., 1997. Volcano geodesy: The search for magma reservoirs and the formation of eruptive vents, *Rev. Geophys.,* **35**(3), 343–384.

Dzurisin, D., 2006. *Volcano Deformation, Geodetic Monitoring Techniques,* Springer-Verlag.

Ebmeier, S.K., Biggs, J., Mather, T.A., Wadge, G. & Amelung, F., 2010. Steady downslope movement on the western flank of Arenal volcano, Costa Rica, *Geochem. Geophys. Geosyst.,* **11**(12), doi:10.1029/2010GC003263.

Ebmeier, S.K., Biggs, J., Mather, T.A. & Amelung, F., 2013. Applicability of InSAR to tropical volcanoes: insights from Central America, *Geol. Soc., Lond., Spec. Publ.,* **380**(1), 15–37.

Feng, L., Newman, A.V., Protti, M., González, V., Jiang, Y. & Dixon, T.H., 2012. Active deformation near the Nicoya Peninsula, northwestern Costa Rica, between 1996 and 2010: interseismic megathrust coupling, *J. geophys. Res.: Solid Earth (1978–2012),* **117**(B6), doi:10.1029/2012JB009230.

Fournier, T., Freymueller, J. & Cervelli, P., 2009. Tracking magma volume recovery at Okmok volcano using GPS and an unscented Kalman filter, *J. geophys. Res.: Solid Earth (1978–2012),* **114**(B2), doi:10.1029/2008JB005837.

Fudali, R.F. & Melson, W.G., 1971. Ejecta velocities, magma chamber pressure and kinetic energy associated with the 1968 eruption of Arenal volcano, *Bull. Volcanol.,* **35**(2), 383–401.

GNV, 1979–2000. *Arenal volcano, Bulletin of the Global Volcanism Network,* Smithsonian Institution, Washington DC.

Grapenthin, R., Freymueller, J.T. & Kaufman, A.M., 2013. Geodetic observations during the 2009 eruption of Redoubt volcano, Alaska, *J. Volc. Geotherm. Res.,* **259,** 115–132.

Gudmundsson, A., Friese, N., Galindo, I. & Philipp, S.L., 2008. Dike-induced reverse faulting in a graben, *Geology,* **36**(2), 123–126.

Gudmundsson, S., Sigmundsson, F. & Carstensen, J.M., 2002. Three-dimensional surface motion maps estimated from combined interferometric synthetic aperture radar and GPS data, *J. geophys. Res.: Solid Earth (1978–2012),* **107**(B10), ETG 13-1–ETG 13-14.

Guglielmino, F., Bignami, C., Bonforte, A., Briole, P., Obrizzo, F., Puglisi, G., Stramondo, S. & Wegmüller, U., 2011. Analysis of satellite and in situ ground deformation data integrated by the SISTEM approach: the april 3, 2010 earthquake along the Pernicana fault (Mt. Etna-Italy) case study, *Earth planet. Sci. Lett.,* **312**(3), 327–336.

Guillaume, S., 2013. Geodetic networks and parameter estimation, Lecture Notes, Institute of Geodesy and Photogrammetry Geodesy and Geodynamics Laboratory, ETHZ, Zurich, Switzerland.

Guillaume, S., Muller, C. & Cattin, P.-H., 2008. *Manuel TRINET+,* 6th edn, HEIG-VD, Département de géomatique, Yverdon-les-Bains.

Herring, T.A., King, R.W. & McClusky, S.C., 2010. *GAMIT Reference Manual, GPS Analysis at MIT,* 10th edn, Department of Earth, Atmospheric, and Planetary Sciences Massachusetts Institute of Technology.

Herubin, C.A., 1978. *Principles of Surveying,* 2nd edn, Reston Publishing Company.

Hofmann-Wellenhof, B. & Moritz, H., 2005. *Physical Geodesy,* Springer.

Hooper, A., Zebker, H., Segall, P. & Kampes, B., 2004. A new method for measuring deformation on volcanoes and other natural terrains using InSAR persistent scatterers, *Geophys. Res. Lett.,* **31**(23), doi:10.1029/2004GL021737.

Jónsson, S., Einarsson, P. & Sigmundsson, F., 1997. Extension across a divergent plate boundary, the Eastern Volcanic Rift Zone, south Iceland, 1967–1994, observed with GPS and electronic distance measurements, *J. geophys. Res.: Solid Earth (1978–2012),* **102**(B6), 11 913–11 929.

Lisowski, M., Dzurisin, D., Denlinger, R.P. & Iwatsubo, E.Y., 2008. *Analysis of GPS-measured deformation associated with the 2004-2006 dome-building eruption of Mount St. Helens,* Washington, US Geological Survey Professional Paper, 1750, pp. 301–333.

Liu, Z., Dong, D. & Lundgren, P., 2011. Constraints on time-dependent volcanic source models at Long Valley caldera from 1996 to 2009 using InSAR and geodetic measurements, *Geophys. J. Int.,* **187**(3), 1283–1300.

Lundgren, P., Berardino, P., Coltelli, M., Fornaro, G., Lanari, R., Puglisi, G., Sansosti, E. & Tesauro, M., 2003. Coupled magma chamber inflation and sector collapse slip observed with synthetic aperture radar interferometry on Mt. Etna volcano, *J. geophys. Res.: Solid Earth (1978–2012),* **108**(B5), doi:10.1029/2001JB000657.

Manconi, A. & Casu, F., 2012. Joint analysis of displacement time series retrieved from SAR phase and amplitude: impact on the estimation of volcanic source parameters, *Geophys. Res. Lett.,* **39**(14), doi:10.1029/2012Gl052202.

Menke, W., 2012. *Geophysical Data Analysis: Discrete Inverse Theory,* Academic press.

Mora, M.M., Lesage, P., Albino, F., Soto, G.J. & Alvarado, G.E., 2013. Continuous subsidence associated with the long-lasting eruption of Arenal volcano (Costa Rica) observed by dry-tilt stations, *Geol. Soc. Am. Spec. Papers,* **498,** 45–56.

Nunnari, G. & Puglisi, G., 1994. The global positioning system as a useful technique for measuring ground deformations in volcanic areas, *J. Volc. Geotherm. Res.,* **61**(3), 267–280.

Palano, M., 2010. Etn@ ref: a geodetic reference frame for Mt. Etna GPS networks, *Ann. Geophys,* **53**(4), 49–57.

Pingue, F., Troise, C., De Luca, G., Grassi, V. & Scarpa, R., 1998. Geodetic monitoring of Mt. Vesuvius volcano, Italy, based on EDM and GPS surveys, *J. Volc. Geotherm. Res.,* **82**(1), 151–160.

Pizarro, D., 1993. Los pozos profundos perforados en Costa Rica: Aspectos litológicos y bioestratigráficos, *Revista Geológica de América Central,* **15,** doi:10.15517/rgac.v0i15.13240.

Pritchard, M.E. & Simons, M., 2002. A satellite geodetic survey of large-scale deformation of volcanic centres in the central Andes, *Nature,* **418**(6894), 167–171.

Reagan, M.K., Gill, J.B., Malavassi, E. & Garcia, M.O., 1987. Changes in magma composition at Arenal volcano, Costa Rica, 1968–1985: real-time monitoring of open-system differentiation, *Bull. Volcanol.,* **49**(1), 415–434.

Rosen, P.A., Hensley, S., Gurrola, E., Rogez, F., Chan, S., Martin, J. & Rodriguez, E., 2001. SRTM C-band topographic data: quality assessments and calibration activities, in *Proceedings of the Geoscience and Remote Sensing Symposium, 2001. IGARSS'01. IEEE 2001 International,* Vol. 2, pp. 739–741.

Samsonov, S. & Tiampo, K., 2006. Analytical optimization of a DInSAR and GPS dataset for derivation of three-dimensional surface motion, *Geosci. Remote Sens. Lett.,* **3**(1), 107–111.

Schmidt, F., 2006. tement tridimensionnel de mesures GPS et terrestres dans les réseaux d'auscultation, *Master's thesis,* HEIG-VD, Département de géomatique, Yverdon-les-Bains, Suisse.

Seube, N. *et al.*, 2012. International cooperation in education: the Vassiviere Erasmus intensive training program (2011–2013) on hydrography and geomatics, in *Proceedings of the Hydro12—Taking Care of the Sea,* 2012 November 13–15, Rotterdam.

Shen, Z.-K., Jackson, D.D. & Ge, B.X., 1996. Crustal deformation across and beyond the Los Angeles basin from geodetic measurements, *J. geophys. Res.: Solid Earth (1978–2012),* **101**(B12), 27 957–27 980.

Shirzaei, M. & Walter, T.R., 2010. Time-dependent volcano source monitoring using interferometric synthetic aperture radar time series: a combined genetic algorithm and Kalman filter approach, *J. geophys. Res.: Solid Earth (1978–2012),* **115**(B10), doi:10.1029/2010JB007476.

Smith, D.A. & Small, H.J., 1999. The CARIB97 high-resolution geoid height model for the Caribbean Sea, *J. Geod,* **73**(1), 1–9.

Soto, G.J. & Alvarado, G.E., 2006. Eruptive history of Arenal volcano, Costa Rica, 7 ka to present, *J. Volc. Geotherm. Res.,* **157**(1), 254–269.

Streck, M.J., Dungan, M.A., Bussy, F. & Malavassi, E., 2005. Mineral inventory of continuously erupting basaltic andesites at Arenal volcano, Costa Rica: implications for interpreting monotonous, crystal-rich, mafic arc stratigraphies, *J. Volc. Geotherm. Res.,* **140**(1), 133–155.

Takada, Y. & Fukushima, Y., 2013. Volcanic subsidence triggered by the 2011 Tohoku earthquake in Japan, *Nat. Geosci.,* **6**(8), 637–641.

Tarantola, A. & Valette, B., 1982. Generalized nonlinear inverse problems solved using the least squares criterion, *Rev. Geophys.,* **20**(2), 219–232.

Torge, W., 2001. *Geodesy,* Walter de Gruyter.

Wadge, G., Oramas Dorta, D. & Cole, P.D., 2006. The magma budget of volcán Arenal, Costa Rica from 1980 to 2004, *J. Volcanol. Geother. Res.,* **157**(1), 60–74.

Wang, H. & Wright, T.J., 2012. Satellite geodetic imaging reveals internal deformation of western Tibet, *Geophys. Res. Lett.,* **39**(7), doi:10.1029/2012GL051222.

Welsch, W., Heunecke, O. & Kuhlmann, H., 2000. *Handbuch Ingenieurgeodäsie. Auswertung geodätischer Überwachungsmessungen,* Vol. 3, Wichmann.

Wendt, J. & Dietrich, R., 2003. Determination of recent crustal deformations based on precise GPS measurements in the Vogtland earthquake area, *J. Geodyn.,* **35**(1), 235–246.

Yang, X., Davis, P.M., Delaney, P.T. & Okamura, A.T., 1992. Geodetic analysis of dike intrusion and motion of the magma reservoir beneath the summit of Kilauea volcano, Hawaii: 1970–1985, *J. geophys. Res.: Solid Earth (1978–2012),* **97**(B3), 3305–3324.

APPENDIX

This appendix describe in more details the transformation to apply to the measurements to be within a topocentric reference system, also called ENU reference system.

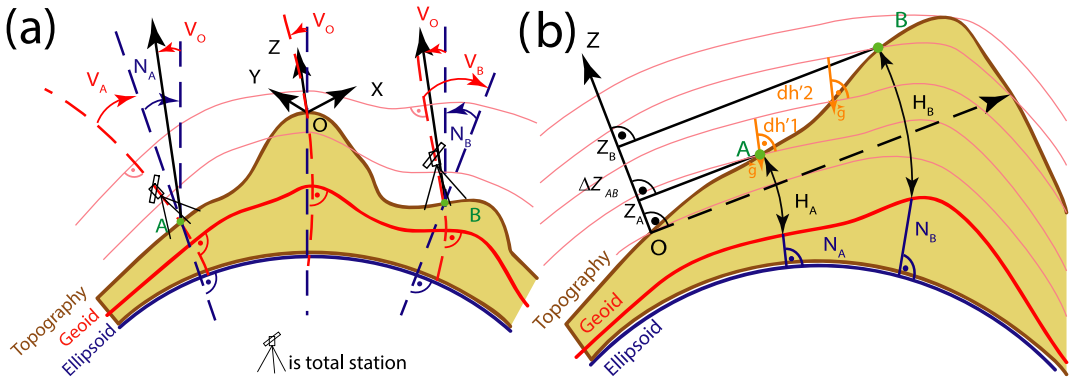

Figure A1. Corrections of (a) angles and (b) height difference observations before an adjustment within a topocentric reference frame (a cartesian reference frame oriented with the direction of the gravity at its origin) (Guillaume *et al.* 2008). The black lines are the topocentric axes, and O the origin of the system. A and B are two sites stationed with a Total Station or levelled. The light red lines are the equipotential surface. The bold red line is the particular equipotential curve at mean sea level called geoid. (a) The dashed red lines represent the direction of the gravity/plumb line always perpendicular to the equipotential curves in light red. The dashed blue lines are the lines perpendicular to the reference ellipsoid in blue. (b) The dh'1 and dh'2 are the levelled differences between I and J. H_i are the orthometric heights. The blue lines are the geoid undulation height N_i. Z_i and δZ_i are the height and height difference in the topocentric reference frame.

Since the topocentric reference system is rigorously Cartesian, GNSS, angles and height differences must be adjusted to compensate for the differences in plumb-line orientation between measurement sites (Hofmann-Wellenhof & Moritz 2005). The transformation of the GNSS measurements within a global 3-D cartesian reference system (e.g. International Terrestrial Reference System, ETRS) consists of three translations and two rotations. The three translation values are the three Cartesian components of the origin of the topocentric system and the two rotations are defined by the value of latitude and longitude of the origin (Guillaume *et al.* 2008).

For angle and heights difference, the differences between the *Z*-axis of a cartesian reference system and the direction of gravity at each site can be divided in three corrections—see Fig. A1(a): (i) the correction of the vertical deflection at the topocentre V_O, (ii) the correction of the angle N_i between the perpendicular line of the ellipsoid surface at the topocentre and the same line at the i point and (iii) the correction V_i, which is the vertical deflection at each site i (Guillaume *et al.* 2008). The corrections (i) (V_O) and (iii) (V_i) are computed in the same way and usually divided in two components (Guillaume *et al.* 2008): η, the north-south tilt and ξ, the east–west tilt. There are three ways to obtain η and ξ: (i) using a precise Earth mass model, (ii) measuring the two components with astronomical geodetic measurements and (iii) computing as parameters in the least square inversion.

The second correction, N_i, is the angle between the direction perpendicular to the ellipsoid at the origin and the direction perpendicular to the ellipsoid at a site. This correction is the largest and correspond to $\sim 1''$ arc degree every 30 m.

As for the angles, levelling measurements must also be integrated in the Cartesian topocentric reference frame, see Fig. A1(b) (Guillaume *et al.* 2008).

(i) The levelled difference $\sum dh_{AB}$ has to be corrected into orthometric difference in height $\Delta H_{AB} = H_B - H_A$ (Torge 2001). This correction depends on the variation of direction and the value of the gravity.

(ii) The orthometric difference heights DH_{AB} are transformed into heights differences Dh_{AB} using the geoid undulation N with $dh_{AB} = DH_{AB} + (N_B - N_A)$.

(iii) The latitude, longitude and ellipsoidal height of both benchmarks within the topocentric coordinate system are transformed to obtain Z_A and Z_B.

(iv) The corrected difference in height is then $\Delta Z_{AB} = Z_B - Z_A$.

The correction is smaller for InSAR, since the horizontal resolution is several metres or tens of metres and the LOS displacement does not suffer much vertical deflection when is small (e.g. a 10 cm LOS displacement has to be corrected by much less than 1 mm if located over 100 km away from the origin of the topocentric system).